2023

Serial sectioning PSOCT and 2PM for imaging post-mortem human brain and neurodeger

BOSTON UNIVERSITY

COLLEGE OF ENGINEERING

Dissertation

SERIAL SECTIONING PSOCT AND 2PM FOR IMAGING POST-MORTEM HUMAN BRAIN AND NEURODEGENERATION

by

SHUAIBIN CHANG

B.A., University of Science and Technology of China, 2018

Submitted in partial fulfillment of the

requirements for the degree of

Doctor of Philosophy

2023

Approved by

First Reader

David A. Boas, Ph.D.
Arthur G. B. Metcalf Chair
Professor of Biomedical Engineering
Professor of Electrical and Computer Engineering

Second Reader

Irving J. Bigio, Ph.D.
Professor of Biomedical Engineering
Professor of Electrical and Computer Engineering
Professor of Physics
Professor of Medicine

Third Reader

Ann C. McKee, M.D.
William Fairfield Warren Distinguished Professor
Professor of Neurology and Pathology

Fourth Reader

Jerome C. Mertz, Ph.D.
Professor of Biomedical Engineering
Professor of Electrical and Computer Engineering
Professor of Physics

Fifth Reader

Lei Tian, Ph.D.
Assistant Professor of Biomedical Engineering
Assistant Professor of Electrical and Computer Engineering

Sixth Reader

Hui Wang, Ph.D.
Assistant Professor of Radiology
Harvard Medical School
Massachusetts General Hospital

DEDICATION

I would like to dedicate this work to my patients Shenghua Zhang and Xuefen Chang, my wonderful sister Sudan Zhang.

ACKNOWLEDGMENTS

I would like to take this opportunity to express my sincere appreciation and gratitude to the following individuals who have played a significant role in the completion of my Ph.D. dissertation.

Advisors:

I am profoundly grateful to my advisor, Prof. David A. Boas for taking me as one of his PhD students and guided me through the past five years with his exceptional knowledge, intellectual stimulation, and comforting sense of humor. He shapes the trajectory of my research and my way of thinking. I want to thank Prof. Hui Wang who is my co-advisor for instructing me with her professional sense of thinking and continuous guidance throughout my trajectory of research. I also want to thank Dr. Ichun Anderson Chen who is like my third co-advisor who has played an important role in directing me to fit in life and research in a different country. I am indebted to them for their invaluable mentorship and the countless hours when they provided constructive feedback and shaping the trajectory of my research, presentation, and way of thinking.

Lab Mates:

I would like to extend my heartfelt thanks to my lab mates, Dr. Jianbo Tang, Dr. Seongwook Park, Dr. Gulce Kureli, Dr. Xiaojun Chen, Dr. Kivilcim Kilic, Dr. John Jiang, Dr. Bernhard Zimmermann, Dr. Dmitry Postnov, Mr. Sreekanth Kura, Ms. Parya Farzam, Dr. Jiarui Yang, Dr. John Thomas Giblin, Dr. Antonio Ortega Martinez, Dr Smrihi Sunil,

Dr. Sharvari Zilpelwar, Dr. Joe O'Brien, Mrs. Anna Novoseltseva, Ms. Bingxue Liu, Mr. Stephen Tucker, Mr. Robert Bing, Mr. Nikola Otic, Ms. Blaire Lee, for their camaraderie, collaboration, and willingness to share ideas. Their support, insightful discussions, and diverse perspectives have immensely enriched my research experience. I am grateful for the stimulating environment they fostered, which encouraged continuous learning and innovation.

Committee Members:

I would like to express my gratitude to my dissertation committee members, Prof. Irving Bigio, Prof. Ann C. McKee, Prof. Jerome Mertz and Prof. Lei Tian, for their valuable guidance, expertise, and constructive feedback throughout the various stages of my research. Their collective insights and scholarly contributions have significantly strengthened the quality and rigor of my dissertation.

Collaborators:

I would like to thank my collaborators who provided great support during my trajectory of research, including the Group of Prof. Shih-chi Chen's at The Chinese University of Hong Kong, the Group of Prof. Irving Bigio's, Group of Prof. Anna Devor's, Group of Prof. Martin Thunemann's at Boston University, Group of Prof. Bruce Fischl's at Massachusetts General Hospital, A.A. Martinos Center, Group of Prof. Francesco Saverio Pavone's in Italy, and Prof. Patrick R. Hof at Mount Sinai,

SERIAL SECTIONING PSOCT AND 2PM

FOR IMAGING POST-MORTEM HUMAN BRAIN

AND NEURODEGENERATION

SHUAIBIN CHANG

Boston University College of Engineering, 2023

Major Professor: Professor David A. Boas, Ph.D., Arthur G. B. Metcalf Chair, Professor of Biomedical Engineering, Professor of Electrical and Computer Engineering

ABSTRACT

The study of Aging and neurodegenerative processes in the human brain necessitates a comprehensive understanding of its myeloarchitectonic, cytoarchitectonic, and vascular structures. While recent computational advances have enabled volumetric reconstruction of the human brain using stained slices, the standard histological processing methods have often led to tissue distortions and loss, making deformation-free reconstruction challenging. Therefore, the development of a multi-scale and volumetric imaging technique that can accurately measure multiple structures within the intact brain would be a significant technical breakthrough. In this work, we present the development of an integrated approach that combines serial sectioning Polarization Sensitive Optical Coherence Tomography (PSOCT) and Two Photon Microscopy (2PM) to provide label-free multi-contrast imaging of human brain tissue. Our method allows for the simultaneous visualization of scattering, birefringence, and autofluorescence properties of the post-mortem human brain. By utilizing high-throughput reconstruction of 4x4x2cm^3 sample blocks and simple registration of PSOCT and 2PM images, we enable comprehensive

analysis of myelin content, cellular information, and vascular structure. PSOCT provides mesoscopic images and enables quantitative measurement of those brain structures, while 2PM provide complementary microscopic validation and enrichment of cellular and capillary information. This combined approach reveals myelin density and structure maps of the whole brain block and supplies intricate vessel and capillary networks as well as lipofuscin-filled cell soma across cortical regions, providing insights into the myeloarchitectural, cellular and vascular changes associated with neurodegenerative diseases such as Alzheimer's disease (AD) and Chronic Traumatic Encephalopathy (CTE).

TABLE OF CONTENTS

LIST OF FIGURES

CHAPTER ONE INTRODUCTION

1.1 Introduction Of Human Brain Myeloarchitecture, cytoarchitecture And Vasculature

The human brain exhibits organization at multiple scales, encompassing both macroscopic and microscopic structures. At the macroscopic level, the brain is divided into regions of gray matter and white matter. Gray matter primarily consists of densely packed neuronal cell bodies, while white matter primarily comprises myelinated axons that form the connectivity highways of the brain. Understanding the spatial arrangement and connectivity patterns of these macroscopic structures is crucial for comprehending overall brain organization and function.

However, to gain a comprehensive understanding of the brain, it is essential to investigate the microscopic components that make up its intricate architecture. Neurons, which are the fundamental building blocks of the nervous system, exhibit remarkable diversity in their morphology, connectivity, and functional properties[1,2]. Neuronal cell bodies, dendrites, and axons form intricate networks, enabling the transmission and processing of information. Other than neurons, microglia, astrocytes and oligodendrocytes etc are also cells found in the brain that provide support, insulation, and protection to neurons[1,3,4]. Mapping the distribution of these cells are fundamental steps to understand the cytoarchitecture of human brain.

Myeloarchitecture focuses on the organization of white matter tracts in the brain[5]. White matter consists of myelinated axons, which are long, slender projections responsible for transmitting electrical signals between different regions of the brain. These axons are surrounded by a fatty substance called myelin, which acts as an insulator, enabling faster and more efficient signal propagation[6]. By examining the patterns and arrangement of these white matter tracts, researchers gain insights into the connectivity and communication pathways within the brain. This knowledge is vital for understanding how different brain regions interact and cooperate to facilitate various functions such as sensory perception, motor control, and higher cognitive processes.

Moreover, the brain's microscopic components also encompass a highly intricate network of vascular structures, namely blood vessels. These vessels, including arteries, veins, and capillaries, are responsible for the delivery of vital oxygen and nutrients to meet the metabolic demands of brain cells. In addition, the vascular network in the brain also plays a role in the regulation of cerebral blood flow[7]. Blood flow to different brain regions can be dynamically adjusted to match the metabolic demands of those regions. This regulation, known as cerebral autoregulation, ensures that each area of the brain receives an adequate blood supply according to its specific needs.

The study of myeloarchitecture, cytoarchitecture and vasculature provides complementary perspectives on the structure and function of the human brain. By combining information about the connectivity patterns of white matter tracts with the distribution of neurons as

well as the vasculature, researchers can develop a more comprehensive understanding of brain organization. This knowledge not only enhances our fundamental understanding of the brain but also has profound implications for neuroscience, psychology, and clinical research. It serves as a foundation for mapping brain networks, investigating the aging process as well as neurological disorders.

1.2 Review of Volumetric Post-Mortem Human Brain Imaging Techniques

1.2.1 Magnetic Resonance Imaging of Post-Mortem Human Brain

Magnetic resonance imaging (MRI) has become a widely utilized tool in neuroscience and clinical practice for its ability to non-invasively map the macroscopic structure of the brain[8–10]. It provides valuable information about the overall organization of gray matter, white matter tracts, and major brain regions. However, one limitation of conventional MRI is its inability to achieve the desired microscopic spatial resolution necessary to visualize and analyze the intricate details of cellular structures within the brain. The resolution limitations stem from various factors, including the size of the imaging voxels and the inherent physical properties of water molecules that MRI relies on for signal detection. As a result, finer structures such as individual neurons, myelinated axon fibers and small vessels and capillaries remain beyond the reach of conventional MRI.

1.2.2 Optical Imaging Techniques for Volumetric Post-Mortem Human Brain Imaging

Comparing to MRI, optical imaging techniques offer much higher resolution from tens of micrometers to sub-micron resolution. However, due to light scattering and absorption in biological tissue, optical imaging techniques are typically limited to a few hundreds of micron imaging depth. To overcome this penetration depth limit, a couple of approaches have been developed.

1.2.2.1 Serial Sectioning and Histology of Post-Mortem Human Brain

Serial Sectioning Histology and Immunohistochemistry are powerful techniques used in the imaging of post-mortem human brain tissue[11], providing detailed insights into the cell types, myelin content, vascular structures, and the pathology associated with conditions like Alzheimer's disease (AD). This method involves the systematic sectioning of the brain tissue into thin slices, typically around 20 to 100 micrometers thick. These sections are then stained using various dyes and immunohistochemical markers to highlight specific cellular components and pathological features. Optical imaging of these thin slices is much easier compared to image thick tissue.

In Serial Sectioning, the brain is embedded in a resin material, allowing it to be sliced into extremely thin sections. Each section is then mounted on a glass slide and stained to enhance cellular structures and contrasts. The stained sections are then digitized using high-resolution scanners, creating a vast dataset of images. Various stain types provide wide

spectrum of choices for staining and imaging of specific cell types, myelin, vessel, and pathological structures such as Amyloid Beta plaque and Neurofibrillary Tangles.

Despite its numerous advantages, serial sectioning histology and immunohistochemistry have several limitations that should be considered. One of the major drawbacks is the laborious and time-consuming nature of the process. Obtaining a comprehensive dataset often requires the cutting and staining of hundreds to thousands of brain sections, which demands significant resources, expertise, and meticulous attention to detail. The complicated process makes it prone to human error at various stages, introducing variability in cutting thickness or staining procedures that can introduce inconsistencies and biases into the results.

Moreover, the process of sectioning, mounting, and staining brain tissue can lead to tissue loss and distortion. Each cutting step introduces the potential for tissue damage, shrinkage, or deformation, which can impact the accuracy and reliability of the resulting histological images, and making 3D reconstruction of volumetric image challenging. Mounting the sections onto slides and staining them also presents challenges, as uneven mounting, folding, or tearing of the delicate tissue can occur, further compromising the quality of the data obtained. These factors collectively make it challenging to achieve accurate volumetric reconstruction of 3D images from histology and immunohistochemistry.

1.2.2.2 Serial Sectioning and Block-Face Imaging

One way to overcome the tissue loss and distortion from the cutting and mounting process is to image the tissue prior to cutting, which is termed as block-face imaging. Serial sectioning combined with block-face imaging is a powerful technique used to study the three-dimensional (3D) structure and organization of biological samples, including brain tissue. This method involves the sequential sectioning of the sample followed by imaging of the freshly exposed block face of the remaining volume, such that the images are free from any distortion. It allows for the reconstruction of high-resolution 3D volumes, providing detailed insights into the cellular architecture and connectivity of the tissue.

In animal brain research, the transgenic process allows for the expression of fluorescent proteins or dyes, enabling structure-specific imaging. However, this approach is ethically impractical for studying the human brain. Therefore, researchers turn to endogenous contrasts as an alternative method for imaging human brain structures and composition. A few different imaging techniques have been combined with serial sectioning for imaging large brain blocks, here we focus on the Polarization Sensitive Optical Coherence Tomography (PSOCT) and Two Photon Microscopy (2PM) and their application in post-mortem human brain imaging.

1.2.2.2.1 Polarization Sensitive Optical Coherence Tomography

Optical Coherence Tomography (OCT) is a non-invasive imaging technique that has revolutionized the field of biomedical imaging, allowing for high-resolution, cross-

sectional imaging of biological tissues in real-time. It provides detailed information about tissue structure and morphology, making it a valuable tool in various medical and scientific applications[12–14]. OCT operates based on the principle of low-coherence interferometry. It utilizes near-infrared light to penetrate into biological tissues, where it is backscattered by different tissue structures. By measuring the interference between the backscattered light and a reference beam, OCT can generate depth-resolved images of the tissue microstructure. This enables visualization of tissue layers, identification of tissue boundaries, and assessment of morphological features with micrometer-level resolution.

One specialized variant of OCT is Polarization-Sensitive Optical Coherence Tomography (PSOCT), which adds an additional dimension of information by measuring the polarization properties of light. This enables the measurement of birefringence, which is the property of certain tissues to alter the polarization state of light as it passes through them. Birefringence can reveal structural and compositional information about tissues, such as myelinated axonal fibers in brain tissue[15–18]. The ability of PSOCT to extract both structural and polarization information from tissues makes it a versatile imaging modality with promising applications in brain imaging.

1.2.2.2.2 Two Photon Microscopy and Endogenous Fluorophores in Human Brain

Two-photon microscopy (2PM) is a sophisticated optical imaging technique that offers several advantages over conventional imaging methods. One notable advantage is its ability to suppress out-of-focus fluorescence, resulting in improved image quality and

enhanced signal-to-background ratio. This feature allows for the acquisition of high-resolution images with excellent clarity and specificity, making it an ideal tool for studying complex biological structures.

2PM has found widespread application in various tissue types, including skin[19,20], retinal[21,22], cancerous tissue[23,24] and brain[25,26]. In the context of brain imaging, the technique has proven particularly valuable. Several endogenous fluorophores present in brain tissue are two-photon excitable, which include the collagen and elastin fibers[27], iron-free variants of hemoglobin[28], and lipofuscin[29] in aging neurons. The presence of these endogenous fluorophores in postmortem human brain tissue presents exciting opportunities for label-free, high-resolution imaging of neurons, capillaries, and axonal fibers in remarkable detail. The label-free imaging of brain tissue using 2PM can complement the information obtained from other imaging modalities, such as PSOCT, providing a more comprehensive understanding of the brain's microstructure and organization.

1.3 Proposal of this Study

In our research, we have made significant progress in the integration of serial sectioning PSOCT and 2PM techniques to image large volume human brain samples at multiple scales. This novel approach allows us to obtain comprehensive information about the brain's microstructure by combining the contrasts provided by scattering, birefringence, and autofluorescence, which allow us to investigate multiple aspects of the brain tissue, including the myeloarchitecture, cytoarchitecture and vasculature. The integration of these

imaging modalities enables a more comprehensive understanding of the brain's structural organization and the interactions between different components.

While previous studies have utilized hybrid systems combining OCT and 2PM in various applications such as wound healing[30], microvascular-flow distribution[31], skin inflammation[20] and skin diseases[24], to our knowledge, no previous work has successfully combined serial sectioning, PSOCT, and 2PM techniques in imaging human brain tissue. Our system is capable of simultaneously imaging and registering key features in human brain, opening a window for investigating their spatial interactions and pathological relevance in brain aging and neurodegeneration.

CHAPTER TWO CONSTRUCTING A HYBRID SERIAL SECTIONING PSOCT AND 2PM SYSTEM WITH VOLUME RECONSTRUCTION WORKFLOW

2.1 Opto-mechanic Design Of Serial Sectioning PSOCT And 2PM System And Realtime PSOCT Data Acquisition And Pre-Processing

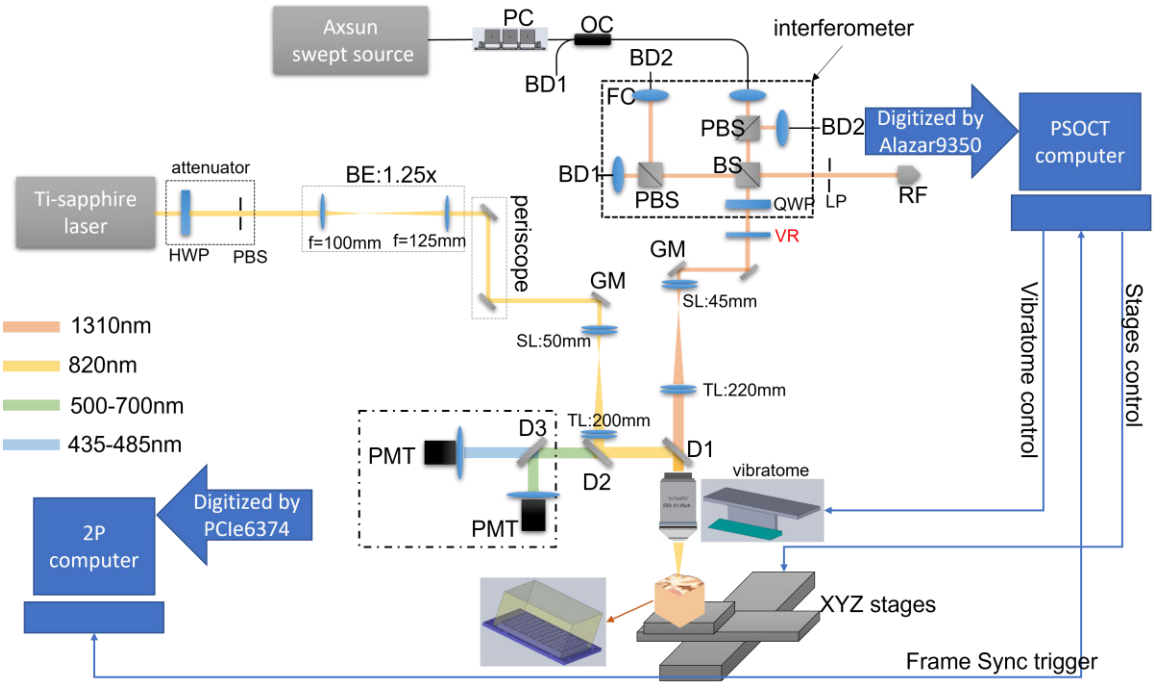

Figure 1 Opto-electric layout of the serial sectioning PSOCT and 2PM system. PC: polarization controller. OC: optical circulator, made from polarization maintaining fiber. BD1-BD2: balanced detector. FC: fiber collimator. PBS: polarization beam splitter cube. BS: beam splitter cube, 50/50 splitting ratio. QWP: quarter wave plate. LP: linear polarizer. RF: retrorelector. VR: electrical variable retarder. GM: Galvano mirror pair. SL: scan lens. TL: tube lens. D1-D3: dichroic mirrors. PMT: photomultiplier tube. HWP: half wave plate. BE: beam expander.

Figure 1 shows the optical and electrical layout of the serial sectioning PSOCT and 2PM system. The hybrid system consists of the PSOCT, 2PM, a custom-built vibratome, XYZ motorized stages, and the control software for the whole system. The PSOCT microscope uses a swept light source (AxsunTech) with 100kHz swept rate, a central wavelength of

1310nm, and a spectral full width half maximum (FWHM) of 110nm, yielding an axial resolution of 5.6 μm in brain tissue (n=1.4). At the interferometer, a polarization controller (Thorlabs Inc) and a polarization beam splitter (PBS) ensure maximum power input with horizontal polarization. A 50:50 beam splitter (BS) separates the light intensity equally onto the sample arm and reference arm. In the sample arm, an achromat quarter-wave plate (QWP) is placed in front of the sample arm at 45 degrees to generate circular polarization on the sample. The scanning path consists of a pair of galvo mirrors (Thorlabs Inc), a 4x telescope and a 4x objective (Olympus, UPLFLN4x, NA=0.13), providing 5 μm lateral resolution and a 150 μm confocal parameter. In the reference arm, a linear polarizer (LP) is placed in front of the reference arm at 45 degrees to make the light intensity equal between horizontal and vertical polarization states. A retroreflector (RF) is placed at the end of the reference arm to back-reflect the light. The back-reflected light from the sample arm and the reference arm interferes when re-combined in the interferometer and is split by two PBS into horizontal and vertical polarization states, which, through balanced detection, result in the co- and cross-polarization measurement of the interference pattern. To acquire the spectrum in even k-space, the k-clock of the light source is fed into a high-speed digitizer (ATS9350, AlazarTech) as a sampling clock. A Graphic Processing Unit (RTX4000, NVIDIA) is used to perform real-time FFT, and the spatial-domain data is trimmed to only save the first 1mm depth. The post-objective power was measured to be 3.7mW, achieving a 95dB SNR in both polarization channels. A 3x3mm^2 FOV was used with 3 μm lateral step size and 10% overlap between tiles.

The 2PM used a Ti:Sapphire mode-locked laser with 80MHz rep rate, 100fs pulse duration and approximately 3W laser power at 820nm. Right after the laser output, an attenuator made of a motorized half-wave plate (HWP) and a PBS was used to modulate the power input to the microscope system. Actual power on the sample was 128mW. Following the attenuator, a 1.25x beam expander combined with the 4X telescope in the scanning path expand the beam size to fill the back-aperture of the objective. The 2PM beam and PSOCT beam in the sample arm were combined using a dichroic mirror above the objective. Sharing the same objective with PSOCT, 2PM achieved a 2 μm lateral resolution and 48 μm axial resolution. The FOV and the imaging speed of 2PM were matched to those of PSOCT, as a result, we used a 2 μm lateral step size, resulting in a 4 μm under-sampling lateral resolution. The depth of focus of PSOCT and 2PM were carefully adjusted to overlap, assuring that they imaged the same region of the brain tissue. However, because 2PM had shorter depth of focus, 2PM only integrated approximately one third of the depth imaged by PSOCT. Two detection channels were available, the short wavelength channel covered from 435 to 485nm and the long wavelength channel covered from 500 to 700nm to capture lipofuscin autofluorescence.

When designing the optical system, a few considerations were addressed:

2.1.1 Why choose UPLFLN4X objective?

Both the PSOCT and 2PM illumination wavelengths are in the near infrared spectrum, with 1300nm and 820nm for PSOCT and 2PM respectively. Consequently, the objective should consider the transmission and chromatic aberration at these wavelength range.

PSOCT and 2PM generally have different requirements for the objective. PSOCT typically uses a low NA objective, sometimes even a scan lens would suffice the requirement, since PSOCT requires a long depth of focus to image over a few hundred of micrometers of depth. However, 2PM usually uses a high NA objective to achieve high spatial resolution and fine optical sectioning along depth. These two contradictory requirements for the objective leads to compromise of NA when selecting appropriate objective.

Another consideration is the field of view (FOV). To reduce the downtime of translating the sample between adjacent tiles, a larger FOV is better, which usually leads to longer focal length and low NA as the clear aperture of an off-the-shelf objective is generally a fixed number.

Considering the above requirements, we pinpointed our choice of objective to two candidates, the UPLFLN4X, which we finally used, and the XLFLUOR4X/340. The XLFLUOR4X is an excellent large FOV objective for two photon imaging, as it achieves 0.28 NA at 5mm FOV, with theoretically 1.0um lateral resolution. And to elongate the depth of focus of PSOCT, we can underfill the back aperture of this objective to achieve a lower effective NA. The UPLFLN4X has lower 0.13 NA, which results in a theoretical lateral resolution of 2.1um. For this one we do not need to underfill the back aperture for PSOCT. Both objectives have good transmission efficiency (>65%) at 820nm, however, none of them specify their transmission efficiency at 1.3um. Measurement at laboratory shows UPLFLN4X has ~70% transmission at 1.3um, while XLFLUOR4X has only 40%

transmission. Lower transmission not only reduce the PSOCT signal intensity, but the reflection at glass-air surfaces within the objective generates strong internal reflection that contaminates the PSOCT images. While it is possible to digitally remove the internal reflections when using a sweep-stable light source, i.e., the start wavelength of each A-scan does not vary too much[32], it is challenging to remove the increased noise at the position of internal reflection. Hence, less internal reflection is better. Due to the lower transmission efficiency and possibly more internal surfaces of XLFLUOR4X, it is not ideal for PSOCT imaging.

The back aperture of this objective is about 20mm, considering the Galvo mirror has 5mm clear aperture, a 4X scan lens and tube lens telescope is needed to fill the back aperture of the objective.

2.1.2 Why using separated Galvo mirror pairs for PSOCT and 2PM?

PSOCT pixel dwell time is fixed to be 10μs as the A-line rate of the swept light source is 100kHz. For 2PM, however, depending on the intensity of autofluorescence and consideration of imaging speed, pixel dwell time is generally less than 10 μs and preferably independently adjustable. Besides, due to the different wavelength used hence the different resolution, 2PM should use shorter step size to achieve higher resolution. Considering the different dwell time and step size, we used two pairs of Galvo mirrors for PSOCT and 2PM.

2.1.3 Why do we need an electrically modulated variable retarder in the sample arm?

The optical components in the sample arm generated a large system birefringence that caused substantial errors in the retardance and optic axis orientation measurements. To address this problem, we used a variable retarder (VR) in the sample arm, assuring the measurement to be pure tissue birefringence. The compensation process can be carried out in 3 steps:

Step1. We imaged a silver mirror and calculated the retardance. Assuming there was no system birefringence, the measured retardance should be 0. So, the none-zero retardance we measured was the accumulated retardance from the optics.

Step2. We set the retardance of the variable retarder to be opposite of the value we calculated in step 1, placed it before the galvo mirrors and rotated it to minimize the signal from mirror in the cross-polarization channel.

Step3. We then fine-tuned the retardance and orientation of the variable retarder iteratively to minimize the cross-polarization channel signal of sliver mirror.

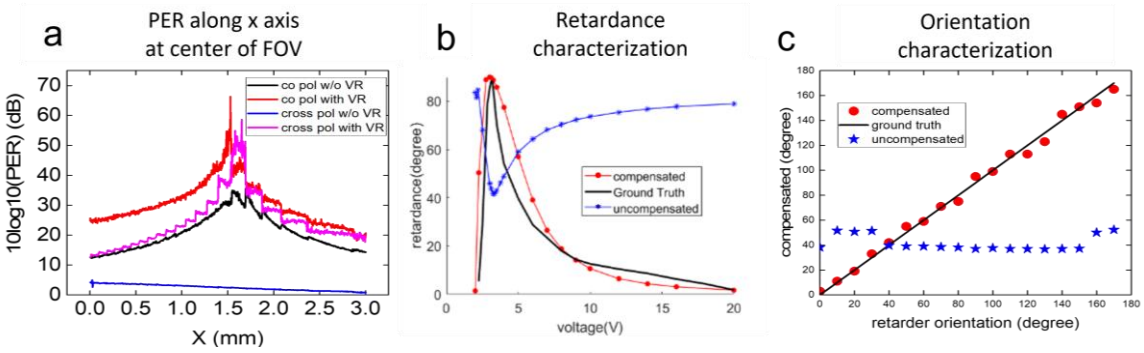

Figure 2 Characterization of polarization extinction ratio (PER), retardance and orientation before and after birefringence compensation using an electrically modulated variable retarder. (a) PER along the x axis at the center of FOV for cross and co polarization channels before and after compensation of birefringence. (b) Retardance measurement before (blue) and after (red) birefringence compensation using a variable retarder as a sample, compared with ground truth (black) of the retardance provided by manufacturer. (c) Comparison of orientation measurement of a retarder as a sample, before (blue) and after (red) birefringence compensation. Black line is the physical orientation of the retarder.

Figure 2 shows a comparison of the polarization extinction ratio (PER), dynamic range of retardance and optic axis orientation before and after system birefringence compensation. Before compensation, the PER (Figure 2.a) of co-polarization channels was below 20dB off the center of the FOV, and the PER of cross-polarization channels was below 5dB. After compensation, PER increased by 10-30dB, recovering PSOCT's ability to measure sample birefringence. Figure 2.b shows the retardance measurement before and after compensation. Before compensation, the hybrid system produced a background retardance of approximately 70° and the measurement on the sample was inaccurate. After compensation, the background was removed and the dynamic range of retardance measurement was recovered to about 90°. The measurement matched to the ground truth of retardance provided by the manufacturer (black line). Figure 2.c shows the orientation measurement before and after compensation. Before compensation, the measurement could not reveal different orientations set on the retarder at all. After compensation, the measured

orientation matched the physical orientation of the retarder and the dynamic range was recovered to 180°.

On the data acquisition side, two high-performance computers controlled the PSOCT and 2P system separately, which were synchronized using frame start and stop triggers. For the 2PM system, we used the ScanImage (Vidirio Inc) to control the 2PM acquisition. For the serial sectioning PSOCT system, we wrote custom software in LabVIEW to serialize the PSOCT imaging, XYZ stages and vibratome slicing. On the data processing side, the data acquisition, FFT, and data saving are parallel processes using the multi-threading of LabVIEW. FFT is carried out in a GPU using CUDA code. PSOCT generated tens of TBs volumetric data, leading to the demand for large storage space and high computing power to process the data parallelly. We established a 10Gb/s Ethernet connection between the PSOCT acquisition computer, a local server with 25TB RAID10 disk space, and the remote Boston University Shared Computing Cluster (BU SCC), with the local server playing as a transfer station that separated the acquisition computer from data saving and transfer. Post-processing was performed on SCC clusters.

To obtain large volumetric imaging, a customized vibratome[33] equipped with a 2.5inch wide sapphire blade was integrated into the imaging system. The vibratome was designed to minimize out-of-plane vibration for optimal cutting performance[34,35]. The cutting thickness was 150 μm and 450 μm, respectively, for non-refractive-index-matched samples and refractive-index-matched samples. With our optimized imaging and cutting scheme and data storage, a 4x4x2cm^3 brain block can be imaged within 6 days.

2.2 Characterization of Optical Performance

We characterized the lateral and axial resolution of both microscopes (Figure 3). Using 1 μm fluorescent beads, the lateral and axial resolution of 2PM was measured to be 2.4 μm and 48 μm, respectively (Figure 3.a, b). The lateral resolution of PSOCT was 5 μm, where the modulation transfer function showed 50% contrast between the line-pair (Figure 3.c). Using the air-glass interface, the axial resolution of PSOCT was measured to be 5 μm (n=1.4 for brain tissue) (Figure 3.d). The depth of focus, i.e., twice of Rayleigh range, was measured to be 150 μm using an intralipid phantom and depth profile fitting (Figure 4.e).

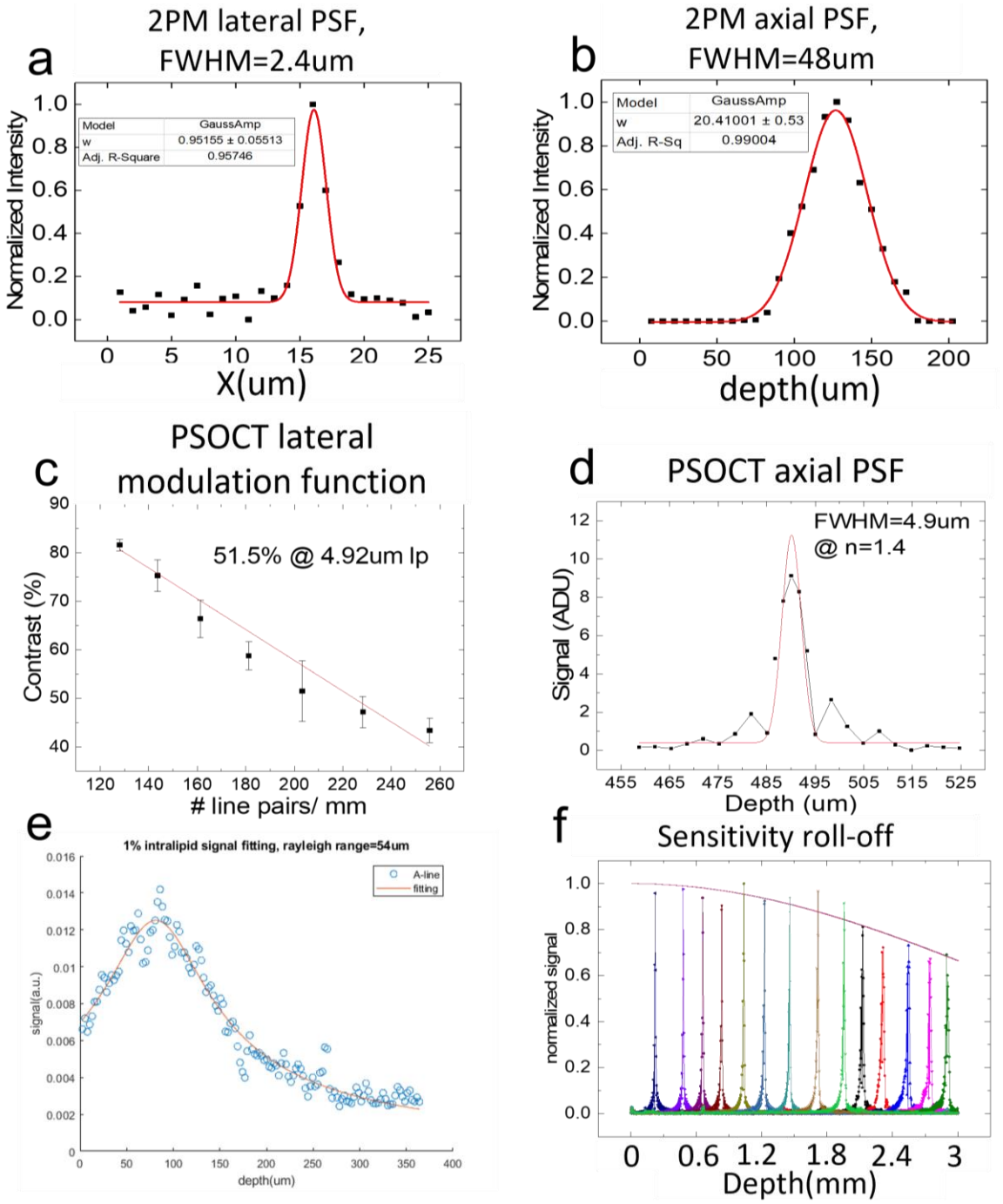

Figure 3 Optical performance of PSOCT-2PM system. (a) lateral resolution of 2PM measured to be 2.4 μm using 1 μm diameter fluorescent beads. (b) axial PSF of 2PM measured to be 48 μm. (c) Lateral modulation function of PSOCT system using airforce target shows 50% contrast at 5 μm line pair. Red line shows linear approximation of theoretical values. (d) Axial PSF of PSOCT measured to be 5 μm using glass slide surface. (e) axial profile of PSOCT signal using 1% intralipid, the fitting of intensity decay shows the Rayleigh range is about 54um, which is half of the depth of focus. (f) Sensitivity roll-off of the PSOCT signal over depth.

In spectral domain OCT and swept source OCT, the sensitivity drops along depth due to the limited coherence length. In spectral domain OCT, it is limited to the spectral resolution of the spectrometer. In swept source OCT, it is limited to the spectral resolution of the swept source. Figure 3.f shows the sensitivity roll-off measurement at different reference mirror positions of our home-built swept source PSOCT. We found the sensitivity remained unchanged over the first 1 mm depth, indicating a long coherence length, which agrees with the manufacture reported 22mm coherence length. The purple horizontal line represented the fitting of the peak intensities using equation 2 in [36]. As the brain signals were captured within the first 1 mm, the small sensitivity roll-off relieved us from performing roll-off compensation during post-processing.

2.3 Characterization of Vibratome Mechanic Performance

Figure 4.a shows the schematic of vibratome sectioning. The sharp blade will cut off the superficial layer of biological tissue, exposing the next layer. As the blade cutting, the curled top layer will undergo tissue loss, damage and distortion that is common to histology process. The tissue surface beneath the blade, however, will have less distortion, and the tissue below surface will have almost zero distortion, which is the part that being imaged during the imaging step of serial sectioning and imaging. Although we claim that the tissue below the surface will have zero distortion, it is under the assumption that the cutting left a flat surface. If the surface after cutting is unflat with dents and bumps, it will affect the imaging and reconstruction. The dents will lower the surface height, requiring us to imaging even deeper. The bumps will increase the distance that light travels in biological

tissue, attenuating the light intensity more. Consequently, for optimal imaging, the flatter the surface the better.

Hence, we adjust the settings of the vibratome to achieve optical cutting performance. We had two vibratomes for testing, the one in Figure 4.b is an old design from our collaborator that uses a rotating motor and an acentric shift to convert rotation into linear oscillation. The motor can be driven from 0 -5000 Rotations per minute, and the amplitude of linear oscillation is about 0.6mm. The one in Figure 4.c is a newer design that uses a linear actuator to directly oscillate the blade linearly. And with a balanced two motor design and LIDAR monitoring of the oscillation, it achieves much less out-of-plane vibration, which should cause less damage to the biological tissue being cut. However, due to the limited range of linear actuator, the amplitude of linear oscillation is about 0.1mm, much less than the older design.

A few other parameters can be adjusted, including the sample feeding rate, which is how fast the stage moves the sample towards the blade, the blade oscillation frequency, and the blade centerline angle. We used human brain tissue as the sample and tested the cutting performance at different parameter settings. The cutting performance is evaluated as the standard deviation of the tissue surface height.

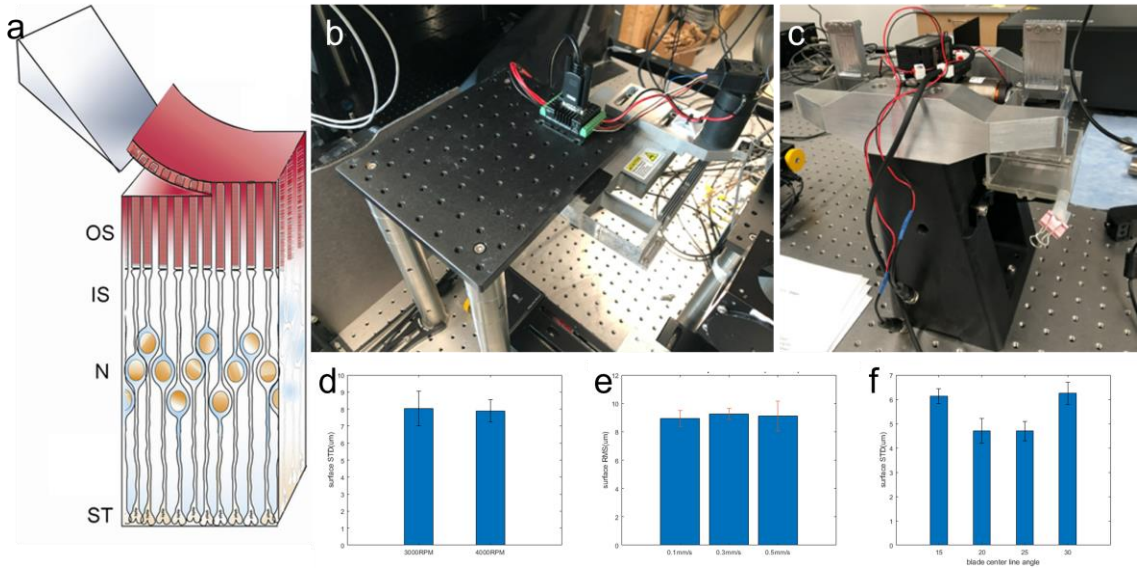

Figure 4 Vibratome performance benchmarking. (a) schematic of the serial sectioning procedure. (b) vibratome version 1, using rotation motor and accentric shaft. (c) vibratome version 2, using linear actuator. (d) comparing vibratome version1 cutting performance at two different oscillation frequency. (e) comparing vibratome version 1 cutting performance at three different feed rate. (f) vibratome 1 performance at four different blade centerline angle.

We tested the vibratome 1 with different parameters settings first. After carefully adjusted the parameters, we found the oscillation frequency and feed rate does not affect cutting performance greatly, but the blade center line angle does affect the result, with 20-25 degree being the best range of cutting angles. We later tested vibratome 2, which performs as good as vibratome 1 on small samples, but for larger samples with more gyrus and sulcus, the cutting performance was quite bad. At the sulcus region, there are large dents and bumps that could vary up to 200um, which will make the imaging and volumetric reconstruction very challenging. After discussing with collaborators in CUHK, we concluded that large oscillation amplitude is necessary for smooth cut with varying sample stiffness, which is large for brain samples white and gray matter. Consequently, all our results are acquired with the vibratome version 1 that has a larger oscillation amplitude.

2.4 Image Correction and Volumetric Reconstruction

The optical distortions can be categorized into three categories. The first two are grid distortion and field curvature distortion, which are geometric distortions along the lateral and axial directions, respectively. The other distortion is the non-uniformity of the intensity across the FOV. Here I describe the steps to calibrate and correct these image distortions.

2.4.1 Geometric Distortion correction

Grid distortion appears as a warped image along the lateral dimensions due to the non-telecentricity of the optical system and is present in both PSOCT and 2PM images. Field curvature distortion appears as a curved depth profile in the OCT B-line image due to the optical path length difference at different scan angles. Since the two geometric distortions depend purely on the optical system, pre-calibration can be applied to correct them.

Briefly, a grid target (Thorlabs Inc) parallel to the table surface was imaged before the experiment. The back-reflection signal off the top surface shared the same field curvature as any well-cut sample. A 2D look-up table of the curvature was obtained from the grid target and applied to the brain images to flatten the signal surface. Next, the average intensity projection (AIP) of C-scan images of the grid target along depth provided the warped image of the grid that was used in grid distortion correction. An ideal grid pattern was generated in MATLAB with the same pixel spacing and orientation as the captured image. Using the UnwarpJ plugin of ImageJ, the warped grid pattern can be registered to

the non-distorted pattern and a transformation matrix was generated that can be used to unwarp the sample images. A similar procedure was applied to correct the 2PM images. Note that for 2PM, a uniform fluorescent glass slide was placed under the grid pattern slide, with the side coated with the grid facing downwards to get a fluorescent grid image.

2.4.2 Intensity distortion correction

The third category of distortion is shading distortion, which appears as non-uniform signal intensity across the FOV due to the vignetting of light beams along the optical system. Shading distortion also present in both modalities. And similarly, as the vignetting is system dependent, the shading distortion will be same for all images, and it could be pre-calibrated and corrected in image processing. Alternatively, Peng et al.[37] developed an algorithm that finds the best correction lookup table for a series of images through an iteration method, which proves to work better than pre-calibration.

2.4.3 Image stitching and volumetric reconstruction

The PSOCT generates speckle-noise contaminated images, which includes the Average Intensity Projection (AIP), Maximum Intensity Projection (MIP), average retardance image, fast axis orientation images, surface height image for vibratome cutting performance evaluation, and volumetric reconstruction. 2PM generates speckle-free autofluorescence images of the two detection channels. As the two modalities were acquired synchronously, the same coordinates could be used to stitch both images. Because 2PM has higher resolution and better SNR, we decided to stitch 2PM images first and apply

the coordinates for stitching PSOCT images. We used the stitching plugin of ImageJ to find the optimal stitching coordinates for the 2PM images. While the XYZ motorized stages we use have good precision and repeatability, there are minor difference of each tile coordinates at different depth. While the most accurate way is to stitch each slice independently and then stitch all slices in Z dimension, for our resolution, simply stacking them would be sufficient. To find the global optimal coordinates, we select three planes that are separated and evenly distributed in depth and merge them into an RGB format. This way, as we run the stitching plugin it will find the optimal stitching coordinates for the three planes in the RGB channels. We can then apply these coordinates to stitch all 2PM images.

Stitching PSOCT images will be straightforward. As PSOCT and 2PM were acquired simultaneously, and all distortions have been corrected in previous steps, PSOCT images and 2PM images will have pixel-to-pixel correspondence except for a pixel size ratio. Hence, stitching PSOCT images and registering them will only require scaling PSOCT and 2PM to the same pixel size and then find out how many pixels were shifted between the two FOVs in X and Y dimensions. Figure 5 shows the overlap of PSOCT and 2PM FOVs. The vessels cross section line plot shows the accuracy of the registration. We determined this shift by finding the maximum overlap between the two images on the same vessel. The scaling factor from PSOCT to 2PM was 1.5. The shift from PSOCT to 2PM was -50 pixels in X dimension and 113 pixels in Y dimension. After applying the inverse of the scaling factor to the 2PM coordinates, we can use the new coordinates for stitching PSOCT images.

The multiple slices can then stack together to generate volumetric reconstruction.

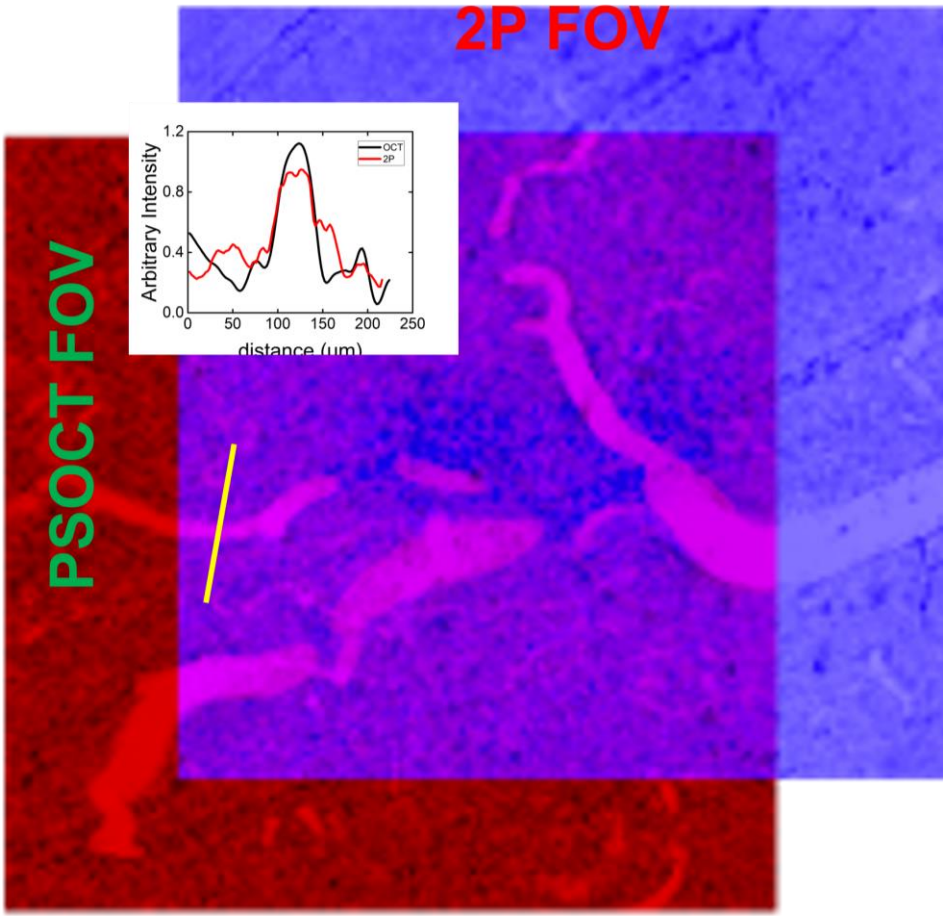

Figure 5 PSOCT and 2PM FOV overlap showing the registration between the two modalities only require linear scaling and linear shift. The inset shows the OCT and 2PM profile of the same vessel for quality of registration.

2.4.3 Correcting the Intensity Depth decay

While the shading distortion is about the intensity non-uniformity along the lateral dimensions, there is another intensity non-uniformity along depth. As light travels deeper into biological tissue, the light intensity attenuates due to scattering and absorption. According to the beer-lambert law, this intensity decay will be exponential, and as we stack multiple slices during volume reconstruction, the intensity along depth will decay to the

end of first slice, and jump up to a large value at the surface of the next slice, and repeating in this fashion as shown in Figure 5.a. This effect is most striking in the white matter where light scattering is strongest.

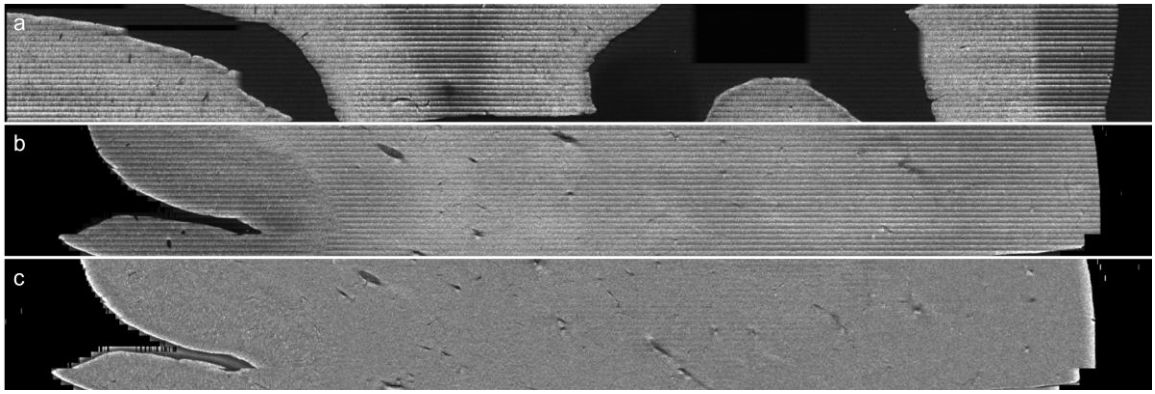

Figure 6 Intensity along depth and two different correction methods. (a) the volumetric reconstruction using raw image intensity, the depth non-uniformity is apparent. (b) Using volumetric scattering coefficient for volume reconstruction, the depth non-uniformity is less intense, but still a few remains. (c) Using high-pass filtering and the volume reconstruction is free from depth non-uniformity, but the white-gray matter contrast is lost as well.

We developed two methods to correct this depth non-uniformity, the first one is based on Vermeer's work[38] of estimating the volumetric scattering coefficient. We then used the volumetric scattering coefficient for volume reconstruction. It greatly reduced the intensity non-uniformity, but there is still some left, as shown in Figure 5.b.

The other method is based on a spatial high-pass filter for each depth to normalize the low frequency background and only leave the high frequency components, which include the vessels, fibers, and tissue boundary. The high-pass filtering is shown in Equation 1:

$$I = \frac{I}{conv(I, kernel)} \qquad \text{Equation 1}$$

where I represents an XY frame of a 3D volume, and kernel was set to be a square all-one

matrix with matrix dimensions to be 500 μm. This empirical matrix dimension was chosen so that it maintained the low frequency component while didn't completely smooth out the sample boundary. After doing this to each XY frame of all slices, there will be no intensity non-uniformity as shown in Figure 5.c. However, a drawback of this normalization is that it also washes away the white-gray matter contrasts. Consequently, this normalization is only used for segmenting the vessel structure from the OCT volume, and we always keep the original intensity for future use.

2.5 Discussion

We have developed a hybrid system that combines serial sectioning PSOCT and 2PM and simultaneously generates multiple contrasts of large volumes of human brain tissue. The optical design of the microscope balances the performances of PSOCT and 2PM systems, allowing them to share a common objective but with different scan scheme for optimizing the imaging parameters. We achieved 5um isotropic resolution of PSOCT and 2.4x2.4x48 um resolution for 2PM, over 3x3mm^2 FOV, which enables the visualization of multiple fine structures at microscopic resolution, all using intrinsic optical properties. The large FOV reduced the imaging down-time during stage translation between tiles, improving the imaging speed and throughput of our system. Additionally, because the two microscopes imaged the same sample simultaneously with largely overlapped FOV, the need for image registration in post-processing was markedly reduced.

For the serial sectioning, we investigated two custom vibratomes, one using rotation motors and acentric shaft and the other using linear actuator. After optimizing the oscillation frequency, feed rate and blade center line angle, we achieved less than 10um RMS of the brain surface cutting. We compared the performance of the two vibratome designs and found that larger oscillation amplitude is an important parameter when cutting non-uniform samples, including brain tissue with white and gray matter having different stiffness.

We developed fully automated acquisition software in LabVIEW that automates the data collection, FFT and pre-processing, as well as saving data onto a remote server with high transfer bandwidth. We also developed a streamline of data processing and reconstruction processes, which correct the geometric distortions and intensity distortions for optical image quality, and utilized the higher resolution and SNR 2PM images for stitching images of both modalities. The reconstructed images enables the investigations of myelin content, vasculature, cells and lipofuscins we discuss in more details later.

Although previous studies have combined OCT with 2PM to enrich the image contrasts of the individual modalities[24,30,31], one of the challenges of combining PSOCT with 2PM is system birefringence that prevents accurate measurement of sample retardance and orientation. System birefringence originates from the optical telescopes, dichroic mirrors, and scanning mirrors, and results in a substantial bias to the polarization measurements of the sample. We removed this bias by using an adjustable retarder that enabled measuring true retardance and orientation from the sample. As a result, we were able to investigate

multiple signals of scattering, birefringence, and autofluorescence from the human brain at different scales. Utilizing these contrasts, we enrichened the measurements of the myelin content, vascular structure, lipofuscin, and neurons in volumetric brain tissue blocks.

CHAPTER THREE LABEL-FREE MEASUREMENT OF MYELIN CONTENT OF POST-MORTEM HUMAN BRAIN

3.1 Introduction

The myelin sheath is a vital component of the nervous system that plays a crucial role in facilitating rapid and efficient transmission of electrical signals along nerve fibers. The composition of the myelin sheath is primarily concentric layers of lipid-rich membranes wrapped around the axon. The organized arrangement and high refractive index mismatch between the myelin layers and the surrounding medium cause the scattering of light[39]. By measuring the scattering properties of brain tissue, researchers can gain insights into the density, thickness, and organization of myelin fibers, providing valuable information about the structural integrity of the nervous tissue.

Birefringence is another important property of the myelin sheath. Birefringence refers to the ability of certain materials, including the myelin sheath, to alter the polarization state of light as it passes through. The myelin sheath exhibits birefringence due to its highly ordered and anisotropic structure[40]. By quantifying birefringence, researchers can gain insights into the organization, orientation, and structural integrity of the myelin fibers.

Traditionally, myelin content can be studied by histology methods such as Gallyas Silver stain[41]. However, the outcome of histology heavily depends on the concentration of the contrast agent, the pH and temperature, and bleaching procedure for undesired pigment,

which may vary across studies. Histology also requires a series of manual processes that are prone to human errors. Consequently, variations from slice to slice are inevitable [42]. In addition, the sample must be cut into thin slices before being stained and imaged, which introduces tissue damage and distortions that are challenging to correct during 3D reconstruction.

Serial sectioning PSOCT, on the contrary, uses intrinsic optical properties of tissue that does not depend on external contrast agents. The scattering coefficient and birefringence measurement is insensitive to system setup, incident power, and acquisition parameters. In volumetric imaging, the images are acquired on block-face prior to slicing, avoiding the vast majority of distortions incurred by tissue cutting and mounting. As a result, serial sectioning PSOCT generates images with consistent qualities across slices and samples. The technique, being automated and robust, is favorable to expand to larger sample size. Thus, serial sectioning PSOCT provides an attractive solution for quantifying volumetric myelin content in the human brain.

3.2 Samples

For the first part of this chapter where we study the relationship between scattering and myelin content, cell density, five brain samples from two human brains from the Massachusetts General Hospital Autopsy Suite (mean age 53.5 ± 12.0 y.o., 1 male and 1 female) that cover the cerebellum, hippocampus, Broca's Area 21, Superior frontal cortex, and somatosensory cortex were used. The brains were neurologically normal without a

previous diagnosis of neurological deficits. These samples and others used in the later study all underwent the standard procedure: they were fixed by immersion in 10% formalin for at least two months [43]. The post-mortem interval did not exceed 24 h. Each sample was embedded in 4% low EEO agarose and was immersed in 1X PBS during imaging.

For the second part of this chapter where we train a deep learning network for virtual Gallyas stain, we used 15 brain samples that were obtained from the Boston University Alzheimer's disease and CTE center, age between 70-90 years, two female, 13 male, 5 of them were late stage AD, 5 of them were late stage CTE, and the rest 5 are age matched normal controls. PMI did not exceed 24 h. Among all the slices we collected from these 15 samples, we selected nine slices that had a good quality Gallyas Silver stain for the training and testing.

3.3 Methods

3.3.1 Obtaining Ground Truth of Myelin Density and Cell Density Using Histology

Histology imaging including Gallyas silver stain and Nissl stain were performed on the slices collected from serial sectioning image. The stained slices were digitized by an 80i Nikon Microscope (Micro- video Instruments, Avon, Massachusetts) with a 4x objective. The pixel size was 1.9 μm.

Gallyas stain and Nissl stain images were normalized in each RGB channel and converted

to mean Optical Density (OD) [42] to represent quantitative measurement of the myelin density and cell density, respectively:

$$OD = \frac{-1}{3} \sum_{i=R,G,B} log_{10}(I_i/255) \qquad \text{Equation 2}$$

where I is the RGB vector of the histology image with I_i representing the intensity of the red, green, or blue channel, respectively. Each RGB channel was normalized separately before converting to OD in log scale. Then the average of three channels was used as the mean OD, which were used as the ground truth measurement of myelin density and cell density.

We also investigated the contribution of cell scattering to the overall tissue scattering using Nissl stain as ground truth of cell density. According to Mie theory [44], the scattering of sphere particles is related to the phase function Q_s, the number density of the sphere N_s, and the cross-section area of the sphere A_s:

$$\mu_s = Q_s N_s A_s \qquad \text{Equation 3}$$

Assuming that the phase function Q_s is constant for all neuron bodies, the scattering coefficient becomes proportional to the product of cellular density N_s and cellular cross-sectional area A_s, which we define as the cellular occupation per area (COPA). From the Nissl stain we calculated the total area occupied by cell bodies and divided it by the total area of the tissue in a small neighborhood to obtain COPA. The computation was conducted in two steps: 1) we segmented the cell bodies in the Nissl stain image using a threshold-

based method, which converts the pixels values inside the cell body to be 1 and the others in the extracellular space to be 0. 2) By calculating the ratio of the number of pixels with value equal to 1 and the total number of pixels within a small neighborhood (roughly 200 x 200 μm box) that moves across the whole image, we obtain the percentage of that local area occupied by cell bodies, i.e., COPA. We did not count cell numbers.

3.3.2 Fitting Scattering and Retardance Properties from PSOCT

By measuring the back-scattered light intensity and polarization, PSOCT enables the measurement of scattering coefficient, back-scattering coefficient, and birefringence properties such as retardance and optical fast axis orientation.

We use the Beer-Lambert Law to model light propagation and attenuation in brain tissue, which is a negative exponential function parameterized by scattering coefficient μ_s and back-scattering coefficient μ_b (Equation 4). The absorption of light at PSOCT wavelength (1.3um) is much smaller comparing to the scattering, hence it is ignored here. The OCT depth profile is also confined by a confocal function h(z) imposed by the objective lens.

$$R(z) = \mu_b' \cdot exp\,(-2\mu_s z) \cdot h(z) \qquad \text{Equation 4}$$

Note that μ'_b is the relative back-scattering coefficient, which includes OCT system parameters such as light power, detector and digitizer configuration and efficiency. We used a simplified Gaussian PSF function to model h(z), which depends on the focus depth

Z_f and the effective Rayleigh range Z_{Rs} of the objective:

$$h(z) = \frac{1}{1 + (\frac{z - Z_f}{Z_{Rs}})^2} \qquad \text{Equation 5}$$

Previously studies that use a four-parameters fitting routine that includes μ_s, μ_b', Z_f, and Z_{Rs} has found strong inter-dependency between these parameters. To untangle the inter-dependency, Yang et al. employed a two-parameters fitting routine by pre-calibrating the Z_f and Z_{Rs} beforehand using 5% intralipid solution sample. In practice, 4.5% agarose embedding can also be used to visualize Z_f and Z_{Rs}. The measured Z_f and Z_{Rs} in agarose can be used as lookup table for fitting μ_s and μ_b' at different location of the FOV. In our system Z_f is a tilting plane with different slopes along X and Y dimensions. In practice, a more general model for Z_f can be a parabolic 2D surface. Z_{Rs} is a constant value across the whole FOV, we used 70 μm.

As Yang et al. found out, Z_f and Z_{Rs} are also affected by μ_s. Higher μ_s resulted in smaller value of Z_f and Z_{Rs}, which they named as effective Z_f and Z_{Rs}. To correct for the scattering dependent change of Z_f and Z_{Rs}, we perform the fitting in two iterations. In the first iteration, we use fixed Z_f and Z_{Rs} and generate the μ_s map over the whole FOV. This μ_s map is smoothed to remove the high frequency component, and then applied to the fixed Z_f and Z_{Rs} with empirically determined ratio. In our system, we used ratio of -1 and -0.5 for Z_f and Z_{Rs}, respectively.

$$Z_{f,effective} = Z_f - \mu_s \qquad \text{Equation 6}$$

$$Z_{r,effective} = Z_r - 0.5 * \mu_s$$

We then used $Z_{f,effective}$ and $Z_{r,effective}$ in the second iteration of fitting for more accurate μ_s and μ_b'.

Traditionally, the OCT depth profile is also affected by the sensitivity roll-off function of the light source, which depends on the coherence length. The wavelength sweeping light source we use (Axsun Inc) has a 22mm coherence length, as our imaging is limited in the first 1mm depth, the sensitivity roll-off within that depth window is negligible, hence no correction of the sensitivity roll-off is needed.

Now the extraction of μ_s and μ_b' reduces to a two-parameters fitting procedure. We fit the measured OCT profile using a nonlinear optimization tool with the least-square error in MATLAB to obtain the optimal solutions for parameters of μ_s and μ_b'. A good fitting generally requires the whole exponential decay, including a long tail. μ_s in gray matter, which is the less scattering tissue type, is about 3-5 mm^{-1}, which corresponds to about 200-300 μm decay length, which is the depth that we used for fitting. To reduce the noise and errors in estimating these optical properties, the OCT A-lines were averaged over a 30 × 30 μm^2 area (10x10 pixels) before fitting, which also help speed up the fitting process by 100 times. We also used 12 × 12 μm^2 area (4x4 pixels) averaging to maintain good resolution that allow us to image large radial fibers and small vessels in these optical

property maps. A ratio map of $\mu_b'/\mu_s$was obtained afterwards for investigating the scatter size using Mie scattering theory.

For the fitting of retardance, as PSOCT measures the accumulated retardance:

$$Ret = \arctan\left(\frac{cross\ pol}{co\ pol}\right) \qquad \text{Equation 7}$$

Which is a linearly increasing model until retardance arrives at the noise level at deeper depth. We used the slope of retardance accumulation as quantitative measurement of the average local retardance:

$$Ret = 2\pi \frac{|n_o - n_e| \cdot z}{\lambda} + b \qquad \text{Equation 8}$$

Where $|n_o - n_e|$ is the absolute value of local retardance, expressed by the absolute difference of refractive index along extraordinary and ordinary optical axis, z is depth in um, λ is the center wavelength in um, b is the background of retardance measurement. Unlike the fitting of scattering properties, for fitting retardance we do not want the noise level at deeper depth as it effectively lowers the fitted retardance. Hence, the fitting depth for retardance is shorter than that used in fitting scattering, which is about 150–200um.

3.3.3 Generalized linear model delineating the relationship between μ_s *and myelin density, cell density*

Taking both myelin density and cell density into account, we examined the quantitative relationship between the optical properties and the Gallyas OD and COPA to reveal the

sources of tissue scattering. PSOCT block-face and the histology images were acquired on slices from the same brain region that were a few millimeters apart. We manually drew 60 to 90 Region of Interests (ROIs) on corresponding slices from both modalities for linear regression analysis. The diameter of circular ROIs ranges from 200 um to 1000 um. The total number of ROIs depends on the number of distinct cortical layers or subdivisions. On average we drew 20 evenly distributed ROIs for each layer in the μ_s, Gallyas OD and COPA maps, respectively.

We built a multivariate, generalized linear model (GLM) for μ_s to include Gallyas OD and COPA as predictors. In the grey matter, we included both Gallyas OD and COPA as contributing factors, whereas in white matter, we only considered Gallyas OD since contribution from neuronal cell bodies was negligible. The GLM relationship can be mathematically described as,

$$\mu_s = X \cdot \beta, \qquad \text{Equation 9}$$

where the matrix X contains the measured Gallyas OD and COPA values and β contains the linear coefficients that will be estimated:

$$X^T = [1\ 1\ \dots\ 1;\ Gallyas\ OD_1\ Gallyas\ OD_2\ \dots\ Gallyas\ OD_n;\ COPA_1\ COPA_2\ \dots\ COPA_n\ ], \qquad \text{Equation 10}$$

$\beta^T = [b\ k_1\ k_2]$ for multi-variable regression. n: number of ROIs

$$X^T = [1\ 1\ \dots\ 1;\ Gallyas\ OD_1\ Gallyas\ OD_2\ \dots\ Gallyas\ OD_n], \qquad \text{Equation 11}$$

$\beta^T = [b\ k_1]$ for uni-variable regression. n: number of ROIs

where k_1 is the slope corresponding to the myelin contribution to the tissue scattering, k_2

is the slope corresponding to the neuronal contribution to the tissue scattering, and b is the contribution from other components, such as scattering from the extracellular matrix. The coefficients were calculated by a pseudoinverse solution as,

$$\beta = (X^T \cdot X)^{-1} \cdot X^T \cdot \mu_s \qquad \text{Equation 12}$$

We used R^2 of Pearson's correlation and Normalized Root Mean Square Error (NRMSE) for examining the goodness of the fitting. Partial correlation coefficient (PCC), two sided t-tests and multiple comparisons were conducted to reveal the significance of the contributions from Gallyas OD and COPA, respectively.

It should be noted that we set COPA in the white matter of all tissue types to be 0 before regression, as there are only glia cells and a few interstitial neurons [45] in the white matter, which won't contribute to scattering significantly. Leaving it unchanged, however, will bias the regression. In the multivariable regression, we also assumed that k_1 and b to be the same in grey and white matter, as we assume that the contribution from myelin and other extracellular components behave similarly, and thus use the same coefficients k_1 and b to describe them jointly.

3.4 Measuring myelin content and cell density using scattering coefficient

3.4.1 Optical property maps resembling quantitative histology

Figure 7 shows the histology and optical property maps for somatosensory cortex. Gallyas Silver stain (Figure 7.a) exhibits contrast among the supragranular layers which consist of

pyramidal neurons, numerous stellate neurons and sparse axons (indicated by blue region), infragranular layers with large pyramidal neurons and axon bundles that connect to the subcortical structures (green region), and the white matter (red region), which mainly consists of highly myelinated axon bundles and glial cells. The Gallyas OD map (Figure 7.b) demonstrate that the supragranular layers have the lowest OD value, followed by the infragranular layers which have intermediate amount of myelinated axon bundles. The white matter exhibits the highest OD value due to the highly myelinated and densely packed axonal bundles. In addition, smaller features can be seen in the Gallyas OD map as well, such as the thin band of denser myelin content at the upper right region of layer IV (red arrow), possibly due to the high-density fibers in the outer band of Baillarger [46]. The Nissl stain and COPA map (Figure 7.c,d) show contrast for cell bodies. The external granular layer (layer II) and the external pyramidal layer (layer III) exhibit the highest COPA value (red region), especially in the lower left part of the sample (black arrow), probably due to the higher neuron density. The internal granular layer (layer IV), internal pyramidal layer (layer V), and the fusiform layer (layer VI) present alternating contrasts (small green arrows). The white matter generally exhibits a low value of COPA, which is mainly attributed to the glia cells.

The μ_s map (Figure 7.e) strongly resembles the Gallyas OD map. The white matter shows highest μ_s because of the highly scattering myelin sheath. As the sparse axon branches into the cortex, μ_s decreases accordingly. The supragranular layer shows the lowest μ_s, due to the lack of myelin content. In addition, the thin band feature at the upper right region

(red arrow) found in Gallyas OD map can also be seen in the μ_s map. Apart from that, the infragranular layers (IV, V, VI) show additional laminar structures (small green arrows) similar to the COPA map but not in Gallyas OD map. Overall, the μ_s map seems to be strongly correlated with myelin content and slightly modulated by the neuron scattering. The μ'_b map (Figure 7.f) offers another feature dimension to aid in discriminating tissue types. It is noticeable that μ'_b varies within the white matter, possibly highlighting fibers oriented within the image plane (green arrow). This is possibly because the fibers oriented within the imaging plane direct more back-scattered photons to the detectors than the fibers oriented through the imaging plane. Consequently, the μ'_b map offers potential information about fiber orientation. The ratio of μ'_b / μ_s map (Figure 7.g) provides another useful feature to distinguish structures in the brain. Similar to the μ'_b map, the ratio of μ'_b / μ_s map also highlights the region with fibers oriented within the imaging plane (green arrow). In addition, the ratio of μ'_b / μ_s map also highlights region of higher value in the superficial layers indicated by the blue arrow, the cause of such contrast requires further investigation. The average intensity projection (AIP, Figure 7.h) is a nonlinear function of the μ_s and μ_b maps, which provides an overall view of the tissue structure for reference.

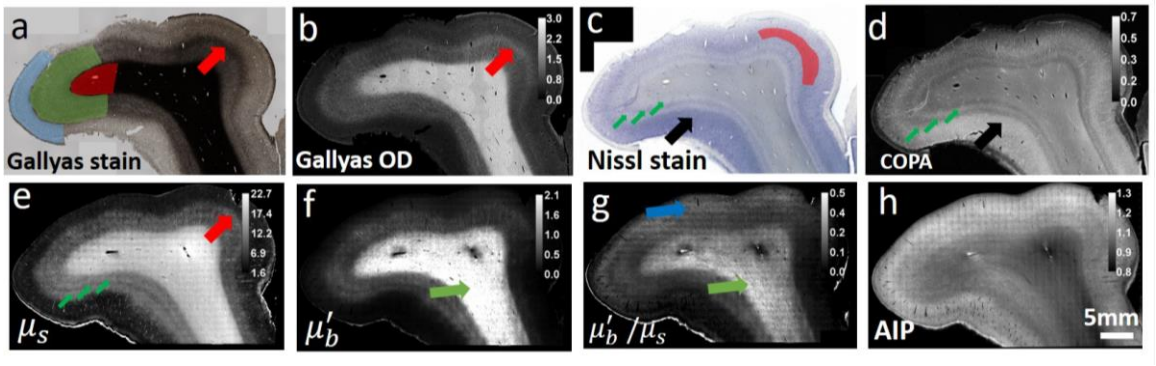

Figure 7 Histology and OCT optical property maps of the human somatosensory cortex. (a) Gallyas Silver stain shows contrast for myelin content. Red region: white matter. Green region: infragranular layers consist of layer IV, V and VI. Blue region: supragranular layers consist of layer I, II and III. Red arrow indicates a thin band of higher myelin content inside layer IV. (b) Optical density (OD) of Gallyas silver stain. The red arrow highlights the myelinated band inside the layer IV. (c,d) Nissl statin and COPA show contrast for cell bodies. The red region indicates the layer II and III with highest COPA value. The big black arrow highlights the high neuron density region. The small green arrows highlight the IV, V, VI layers within the infragranular layer with alternating contrasts. (e-g) Optical properties derived from the OCT images. (e) μ_s map. Small green arrows highlight the alternating contrasts in the infragranular layers similar to that in the COPA map, and the big red arrow indicates the myelinated band seen in Gallyas OD map. (f) μ'_b map. Green arrow highlights the fibers with high intensity, possibly oriented within the imaging plane. (g) Ratio map of μ'_b/μ_s. Green arrow highlights the fibers with high intensity, similar to that in the μ'_b map. The Blue arrow highlights the region with high signals in the supragranular layers. (h) AIP image.

3.4.2 The relationship of scattering coefficient and myelin content

The similarity between the μ_s and Gallyas OD maps indicates that myelin is a crucial factor contributing to the brain tissue scattering. To quantitatively inspect the relationship, we plot μ_s versus Gallyas OD in selective ROIs, which covered all the laminar layers as well as the white matter for the five brain regions. The scatter plots indicate a strong linear relationship between scattering coefficient and Gallyas OD, which is consistent with the Mie theory [47]. Therefore, we fit the data with a linear model and presented the results in Figure 8. Remarkably, the five samples share similar linear relationships as indicated by the

slope parameter (k_1) of the fitting results, although individual samples have distinct patterns of μ_s and Gallyas OD distributions. In the cerebellum (Figure 8.a), data points from the white matter, granular layer and molecular layer form three discrete clusters. However, they all follow a shared linear function (k_1 = 5.79) in which higher Gallyas OD is associated with higher μ_s. Similar patterns are observed in the somatosensory cortex (Figure 8.c), where the six cortical layers and the white matter group into three clusters and share a co-linear relationship (k_1 = 7.48). Supragranular layers (layer I, II and III) form a cluster with the lowest Gallyas OD and μ_s, infragranular layers (layer IV, V and VI) form a cluster with intermediate values, and the white matter cluster exhibits the highest values. The other two cortical regions of SupFrontal and BA21 (Figure 8.d-e) only present two discrete clusters. The supragranular layer and infragranular layer in both regions fall into a single cluster with low Gallyas OD and μ_s. The white matter tracts show high values close to those of somatosensory cortex. Interestingly, the SupFrontal displays a within-cluster trend in both grey matter and white matter, suggesting a myelin gradient across cortical layers. Regardless, the slope parameters (k_1 = 8.57 for SupFrontal and k_1 = 6.24 for BA21) demonstrate a similar relationship as those revealed in the cerebellum and the somatosensory cortex. In the hippocampus (Figure 8.b), due to complex anatomical structures, data points from different layers form a continuous distribution. For example, the fimbria, white matter and fornix show gradually increasing Gallyas OD and μ_s values, while having large overlaps with the CA4 and dentate gyrus. Despite the different distribution pattern from other tissues, the fitting result is comparable with a slope parameter k_1 = 8.26.

An extraordinary linear relationship between Gallyas OD and μ_s is revealed in all the samples ($P<10^{-10}$) with high correlation coefficients (PCC>0.85 for all brain regions, see Figure 9.b). The slope between Gallyas OD and μ_s falls in a narrow range of 5.8 to 8.6. Slope variations are possibly due to different staining backgrounds, as well as other scattering factors such as neuronal cell bodies. In Figure 8.f we combined all the data from the 5 samples and fit a single linear function, which reveals an average slope of 7.2 (correlation coefficient= 0.936, $P<10^{-60}$). These results provide evidence that the linear relationship between optical scattering and myelin content holds in different regions of the brain. Therefore, scattering coefficient may potentially be used as an objective measurement of the myelin content in the human brain.

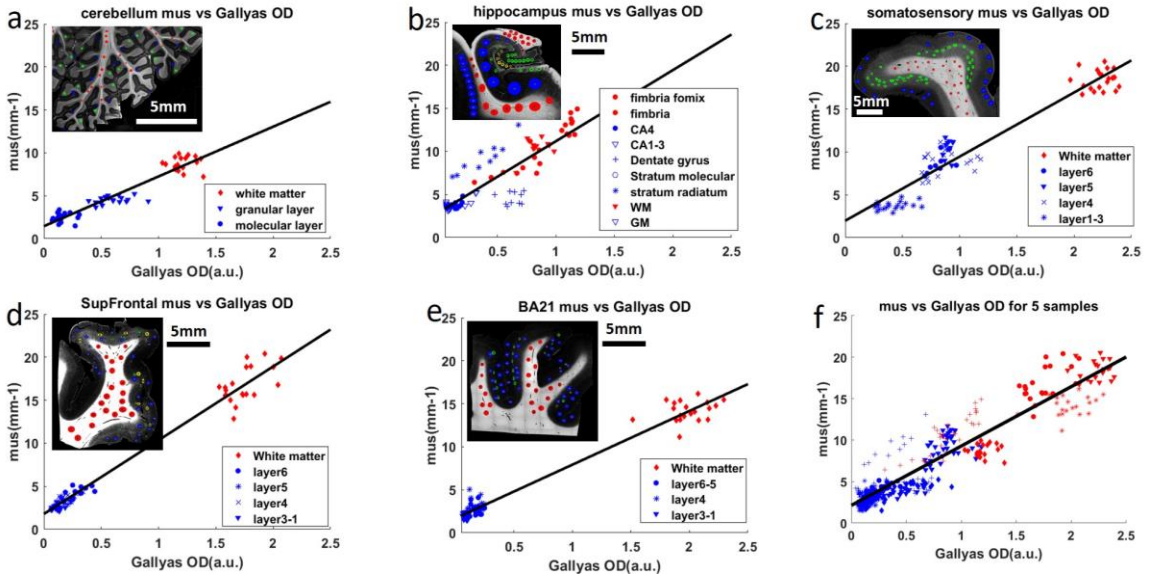

Figure 8 (a–e) Linear regression of μ_s and Gallyas OD for 5 different regions in human brain samples. Red dots: white matter data points. Blue dots: grey matter data points. The inset figure shows the Gallyas OD map of the corresponding sample. The Red circles in the inset figure represent the ROIs in the white matter. The blue, green and yellow circles represent the ROIs in different layers of the grey matter, for example, the green ROIs in (c) represent infragranular layers and the blue ROIs represent the supragranular layers. (a) cerebellum. (b) hippocampus. (c) somatosensory cortex. (d) Superior frontal cortex (SupFrontal). (e) middle temporal Brodmann area 21(BA21). (f) linear regression of all data points from 5 samples. The six panels have the same range on the X and Y axes for easier comparison.

3.4.3 The relationship of scattering coefficient and joint myelin content and neuron density

The results of the linear model in session 2.2 suggest that myelin is a strong predictor of scattering coefficient in both grey and white matter of the human brain. In the cortex, neuronal cell body is another factor that should be taken into consideration when interpreting the scattering coefficient of the brain tissue. In this section, we first re-evaluate the relationship of μ_s and Gallyas OD by including the factor of COPA. Next, we quantify the correlation between μ_s and COPA to examine the cell body contribution in scattering.

Figure 9.a compares the slopes for Gallyas OD (k_1) in univariate regression where only Gallyas OD was considered, and multivariate regression where COPA was included as well. We found that k_1 values were highly comparable between these two models with differences less than 10% in all brain regions Besides, the partial correlation coefficient (PCC) of Gallyas OD in the multivariate regression (Figure 9.d) was found higher than 0.9 for four out of five samples ($P<10^{-10}$ for all), with a slightly lower PCC of 0.6 in the hippocampus. Compared to the univariate regression, the partial correlation coefficient in the multivariate regression has only minor difference in most samples. The consistency of k_1 in the two analyses reinforces that the linear relationship between μ_s and Gallyas OD largely preserves even when cell body scattering is taken into account. The high PCC in multivariate model consolidate the finding in session 2.2 that μ_s is strongly correlated with myelin content across brain regions. In addition, when evaluating the R^2 of Pearson's correlation and Normalized Root Mean Square Error (NRMSE, Figure 9.c, d) for the

regression, we found that adding COPA into the model only results in small improvements, which indicates that myelin content is a dominant factor to scattering coefficient.

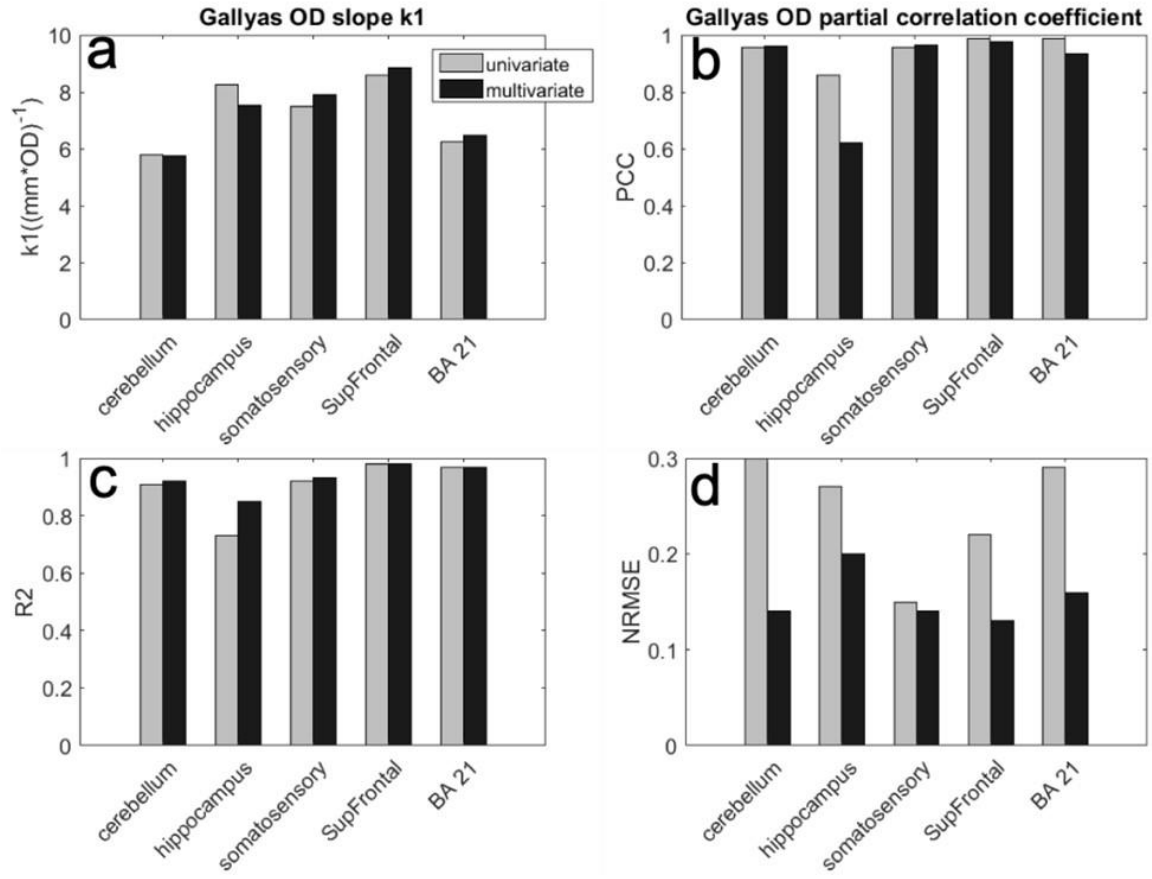

Figure 9 Multivariate regression of μ_s vs Gallyas OD and COPA (grey bars), compared against univariate regression where only Gallyas OD is considered (black bars). (a) Gallyas OD slope k_1 of 5 brain regions resulted from univariate regression and multivariate regression. From left to right: cerebellum, hippocampus, somatosensory, SupFrontal and BA21. (b) Correlation coefficient with Gallyas OD in univariate and partial correlation coefficient in multivariate regression. (c) R^2 of Pearson's correlation in univariate and multivariate regressions. (d) Normalized root mean square error (NRMSE) of univariate and multivariate regressions.

Figure 10 elaborates the correlation between μ_s and COPA in the multivariate regression model. The slope for COPA (k_2) exhibits large variations across the 5 different samples (Figure 10.a). In somatosensory cortex, Supfrontal and BA21, a positive k_2 was found,

while in cerebellum and hippocampus, k_2 was negative. Two-sided t-test reveals a significant positive correlation only in the somatosensory region (P<0.01, PCC=0.45). The correlations in SupFrontal and BA21 are moderate (Figure 10.b), but further statistical test fails to find a significance (P=0.11 for SupFrontal and P=0.35 for BA21). These results suggested that the neuronal scattering is a small contribution to the overall scattering coefficient and the effect varies across the brain. The negative correlation in the cerebellum and hippocampus was counterintuitive. However, it should be noted that the size of neurons in densely packed layers such as the granular cells in the cerebellum and the dentate gyrus in the hippocampus is much smaller than that of the other layers, which leads to a reduced scattering coefficient. The intercept in the multivariate regression exhibits large variation as well (Figure 10.c). As the intercept in the regression encompasses the unmodeled components to the tissue scattering, such as the extracellular matrix, the small intercepts in hippocampus, somatosensory, and BA21 indicate a negligible contribution from these remaining components. However, in cerebellum and SupFrontal cortex, we found a significant intercept (P<0.001), indicating substantial scattering components remained. Overall, the fitting results for COPA in the model are coherent with findings in session 2.2 and 2.3 that μ_s is dominant by the myelin factor. Neuronal cell body, however, only plays a secondary contribution to tissue scattering in the human brain.

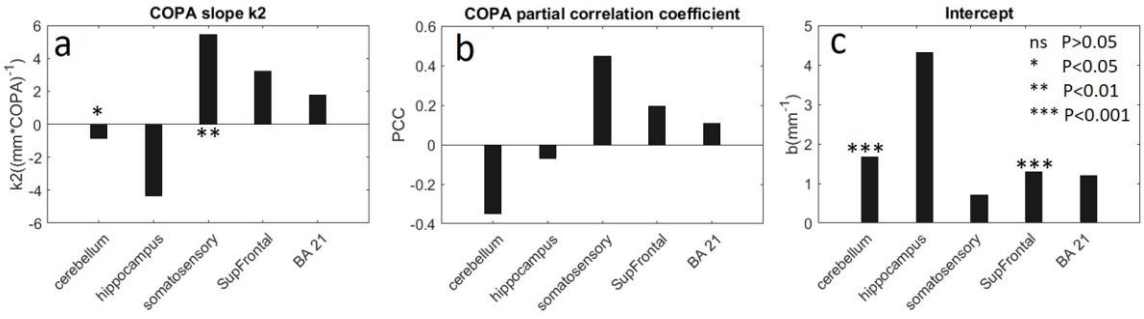

Figure 10 Evaluation of μ_s with COPA and remaining factors in multivariate regression. (a) COPA slope k_2 in the five brain regions. Regions with stars indicate significant k_2. (b) Partial correlation coefficient of COPA with respect to μ_s. (c) Intercept b of the multivariate regression in the five brain regions.

3.5 Virtual Gallyas Staining Using Digital Transferred Scattering Coefficient

We have found that μ_s is strongly correlated with the myelin content and that linear relationship is maintained across different regions of the brain. The domination of myelin content in tissue scattering is reasonable considering the high index of refraction of myelin (n=1.47[48]) with respect to the surrounding aqueous environment (n=1.35). The results from our study suggest that μ_s obtained from OCT imaging can be used as a robust predictor for myelin content of the human brain. However, the community of neuroanatomy has been using histology methods such as Gallyas Silver Stain for decades to measure myelin content, to persuade them to adopt our method, we believe it is beneficial to convert our μ_s maps into virtual Gallyas stain images.

A direct way would be using the linear relationship that we discovered and convert μ_s maps into virtual Gallyas OD maps, then reverse the calculation steps of Gallyas OD maps to make it look like the brownish Gallyas stain images. There are two drawbacks in this

direction, the first is the deviation of the relationship from linear function, as can be seen from the broadened distribution of samples in Figure 8.f. This deviation will eventually lead to the limited correctness of the virtual Gallyas stain images. Secondly, we averaged the three RGB channels when calculating the Gallyas OD value. As we are reversing these steps, we'll have to assume the equal value for RGB channels, which is not necessarily true for Gallyas Stain.

In the past few years, deep learning methods have revolutionized the field of Digital Staining (DS), which aims to transform label-free images into histological staining-like images using a computational model[49]. DS offers a fast and low-cost alternative to conventional Physical Staining methods. Several DS models have been developed that transform different pairs of input-output imaging modalities. Here, we collaborated with Dr. Shiyi Chen from Tian lab at Boston University to develop semi-supervised learning framework for generating virtual Gallyas stain images using a limited amount of weakly paired Gallyas stain and μ_s images.

Figure 11 shows three samples that were imaged by OCT and generated μ_s maps, which was digitally transferred to virtual Gallyas stain using our developed Deep learning model and compare with real Gallyas Silver stain images from adjacent slices. The first row shows a sample which virtual and real Gallyas stain shows comparable contrasts at the white-gray matter boundary and the myelin bands in the gray matter as indicated by the red arrows. While the Virtual Gallyas stain has more uniformity artifacts in the white matter, it shows

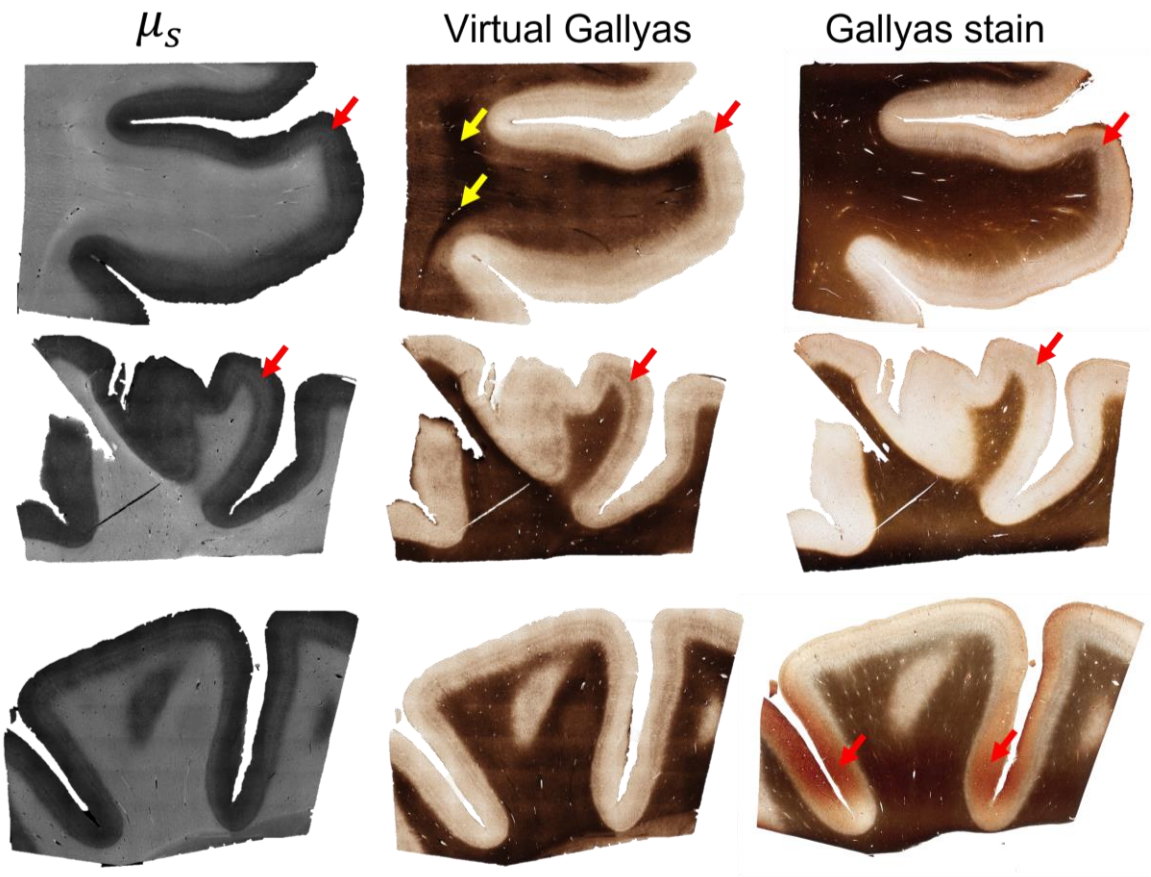

Figure 11 Three samples showing the comparison of μ_s maps, virtual Gallyas stain and real Gallyas stain comparison. Red arrows show the cortical layer contrast. Yellow arrows show the deep white matter contrast.

the denser myelin structure beneath the sulcus (yellow arrows) that are not seen in the Gallyas stain. The second row shows a sample which virtual Gallyas stain shows stronger cortical layer structures than the real Gallyas stain image, as indicated by the red arrows. The real Gallyas stain may experience shorter impregnation time that resulted in the weaker appearance of cortical layers. The third row shows a sample which real Gallyas stain shows redder cortex as indicated by the red arrows, which may have resulted from the insufficient washing steps during the histology process, while the virtual Gallyas stain is free from that artifacts. These examples demonstrate that Virtual Gallyas stain from μ_s maps using our

proposed deep learning model can achieve as good as quality as real Gallyas stain, sometimes with even more uniform contrasts and stronger contrasts of the cortical myelin layers.

To further demonstrate the generalization capability of our trained DS model, we applied it to hippocampus that has not been seen during the training. Figure 12 shows the anatomy of hippocampus, virtual Gallyas stain, Nissl stain and real Gallyas stain of adjacent slices. On a large scale, DS successfully transform the image contrast matching the anatomical structures of hippocampus anatomy. By comparing with the anatomy of hippocampus[50], we can find the alveus and/or fimbria fornix layer on top, the CA1–CA4 regions, and the stratum radiatum under CA2 and other structures as well. What's impressive is that in CA1–CA4 regions we found brown spots in virtual Gallyas image, which, after comparing with Nissl stain, are highly likely individual neuron somas. The Dentate Gyrus, which is a thin layer of cells, is also visible in the virtual staining, although not as strong contrast as in the histology images. The reason why cells especially neurons in the CA1–CA4 regions are visible in virtual staining but not in cerebral cortex regions is worth investigating. It may be a result of the large neuron size and simpler Extra cellular matrix composition in the hippocampus. Regardless, the contrast of neuron in the hippocampus using PSOCT scattering maps and digital staining suggests interesting application of our method to study the cell loss in the hippocampus during neurodegenerative diseases such as Alzheimer's disease.

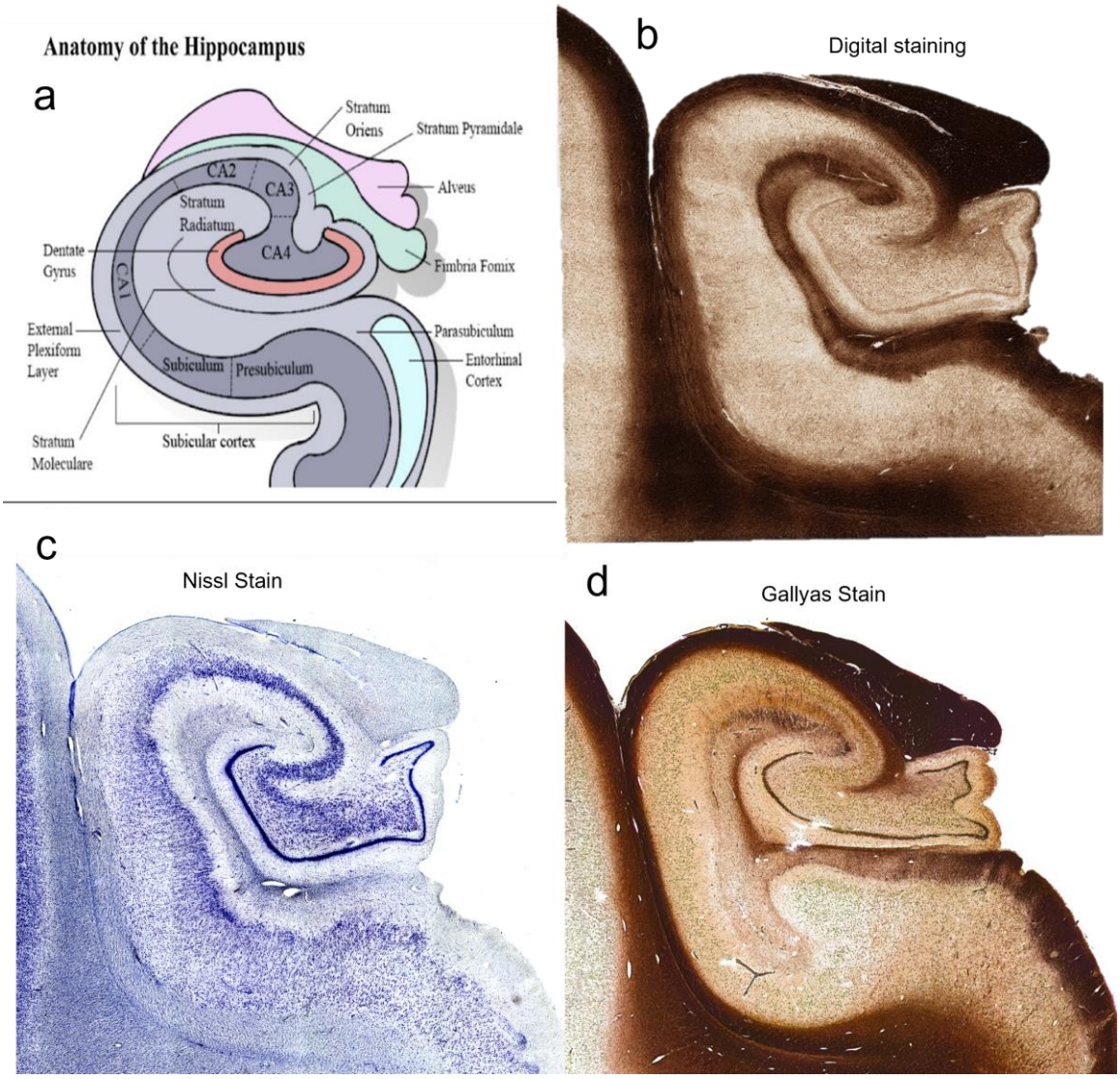

Figure 12 Comparison of anatomical structures in the digital Gallyas stain, real Gallyas stain and Nissl stain. (a) hippocampus anatomy, reprint from Pang et al., Ammon's Horn 2 (CA2) of the Hippocampus: A Long-Known Region with a New Potential Role in Neurodegeneration. (b) virtual Gallyas stain. (c) Nissl stain of adjacent slice. (d) Real Gallyas stain of adjacent slice.

3.6 Retardance and Back-Scattering Reveals Fiber Crossing

Other than μ_s, μ'_b and retardance also provide insights about the fiber structures, especially where multiple directions of fibers crossing each other. Figure 13 shows the comparison of μ_s, μ'_b, retardance and orientation of two samples. The first row used a

sample that was imaged in 1X PBS. Comparing to μ_s map, μ_b and retardance show slightly darker contrast beneath the two sulci, as indicated by the arrows. The orientation image was affected by system bias, which shows as repetitive green pattern. Still, it can be vaguely seen that beneath the two sulci that the fibers are bending along the cortex. To remove the artifacts in orientation as well as to strengthen the retardance contrast, we used another sample with index matching in 60% glycerol, shown in the second row of Figure 13. With remaining scattering, μ_s and μ'_b still shows the white-gray matter contrast but the gray matter signal is reduced. With index matching, light can penetrate deeper and the accuracy of fitting retardance can be improved, after which we find clear darker regions in the retardance image, similarly, beneath the sulcus in the white matter as highlighted by the arrows. We also used smaller FOV to reduce the artifacts in orientation, which allows us to see the fiber orientation much clearer. Fiber orientation clearly displays the turning of fibers at the region with darker retardance.

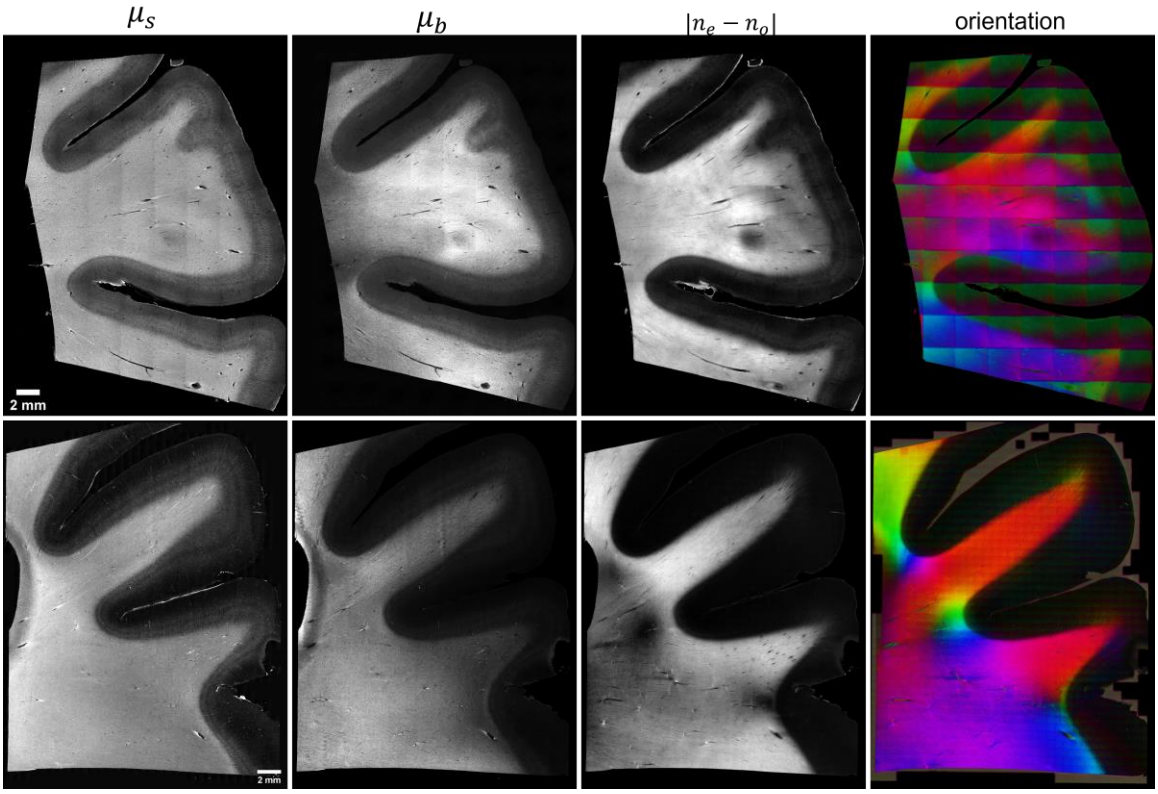

Figure 13 Two samples comparing the μ_s, μ'_b , retardance and orientation. First row: a sample imaged in 1X PBS, 3x3mm FOV. Second row: a different sample index matched using 60% Glycerol, 1x1mm FOV.

Consequently, while μ_s only gives contrasts about myelin density, both μ'_b and retardance provide measurement of fiber structures, especially at the sub-sulcus white matter where fibers are turning along the cortex surface and crossing each other. Between retardance and μ'_b, retardance provides higher contrasts of the fiber structure, especially with index matching. Besides, orientation map can be used to validate the fiber structure as well.

3.7 Use 2PM as microscopic validation of PSOCT measurements

μ_s, μ'_b and retardance provide complementary information of myelin structure and density. In Figure 14.a–c we compared the estimated μ_s, μ'_b and retardance for the same

slice of the tissue block. Comparing these optical properties, we found all of them manifest a higher value in the white matter compared to the grey matter, owing to densely packed myelin content. We also found some differences among the three contrasts in the white matter, as indicated by the blue arrows and dashed rectangular ROIs. In these regions, μ_s shows opposite local variation comparing to μ_b' and retardance. Take the blue dashed ROIs for examples, μ_s shows reduced scattering while μ_b' and retardance shows increased contrasts at this sub-sulcus white-gray matter boundary. The microstructure of fibers underlying those optical property differences can be identified with high-resolution 2PM imaging. Zooming in to the higher resolution images of 2PM (Figure 14.d), we found the autofluorescence image highlights parallel U-fibers (yellow arrows) turning along the sulcus. This well-organized structure of the U-fibers could enhance the birefringence. In addition, the high μ_b' was concordant with previous studies[51] showing that μ_b' highlights small fiber tracts that were parallel to the imaging plane. For the red ROI in deep white matter, it was evident that the μ_s was higher than the surrounding area. Zooming into the corresponding area in 2PM (Figure 14.e), we found multiple large fiber tracts that obliquely ran through the imaging plane. Considering the strong scattering of densely packed fibers, the same structure may be the microscopic origin of the increased μ_s value. In short, our hybrid system allowed for the extraction of birefringence, μ_s, and μ_b' from the same slice as well as the microscopic validation of the mesoscopic measurements using 2PM.

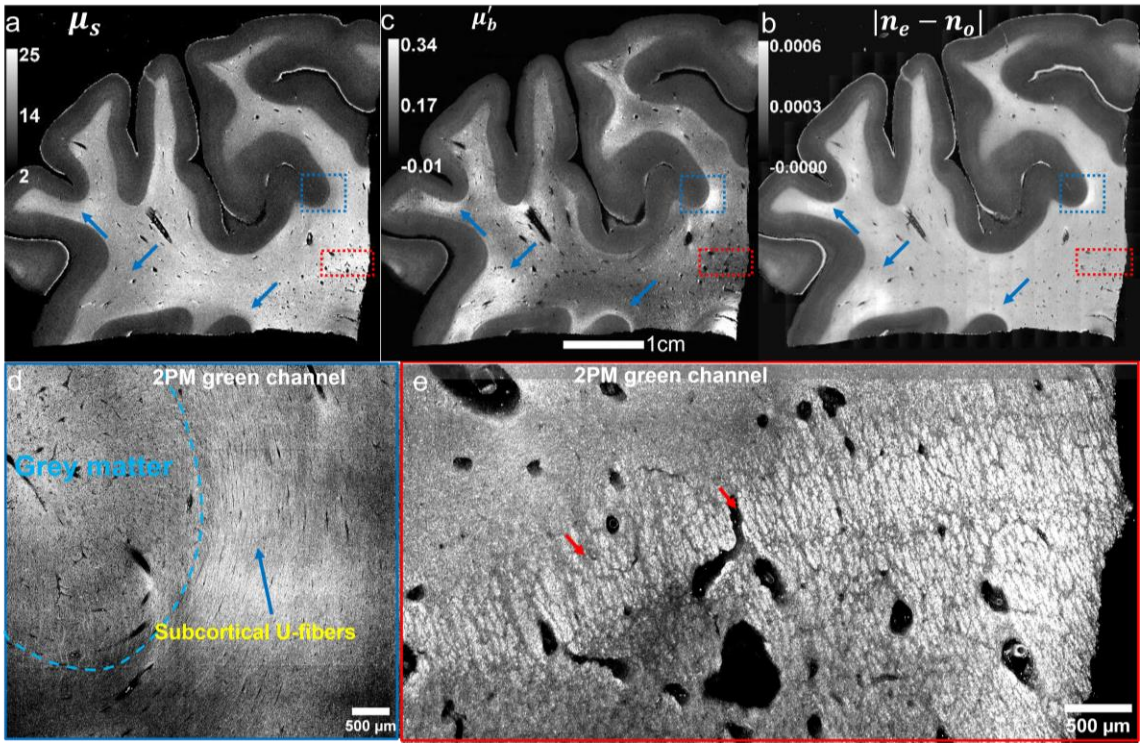

Figure 14 2PM provides microscopic validation of PSOCT measurements. (a-c) μ_s, μ'_b and retardance of the same slice, the blue arrows and dashed ROIs highlight regions where the three properties show different contrasts. (d) zoom in of the blue ROI region where the parallel U-fibers can answer the different contrasts in the PSOCT properties. Similarly, (e) zoom in to the deep white matter region in red ROI and reveals the density packed fiber tracts that answer the different contrasts of the three PSOCT properties.

3.8 Measuring demyelination in aging process

Based on the quantitative measurement of myelin content using these different optical properties, we applied it to study the demyelination process in aging. Figure 15 shows the comparison of μ_s and retardance in the white matter and gray matter separately. We found there are increased μ_s but decreased retardance in both white and gray matters of the older age group. We think the decrease of retardance is a result of myelin breakdown, leading to less organized myelin sheath, while the increased scattering is the result of brain atrophy and remained scattering from the myelin defects that are not efficiently

cleared out.

Right now, we have only three samples in this result. A few other normal control samples were not included because they have more than 24 hours of post-mortem interval (PMI), which as we are working to investigate more, have vicious effects on the myelin sheath to cause it to degenerate more. Another future step is to include different age groups so a regression analysis will be possible.

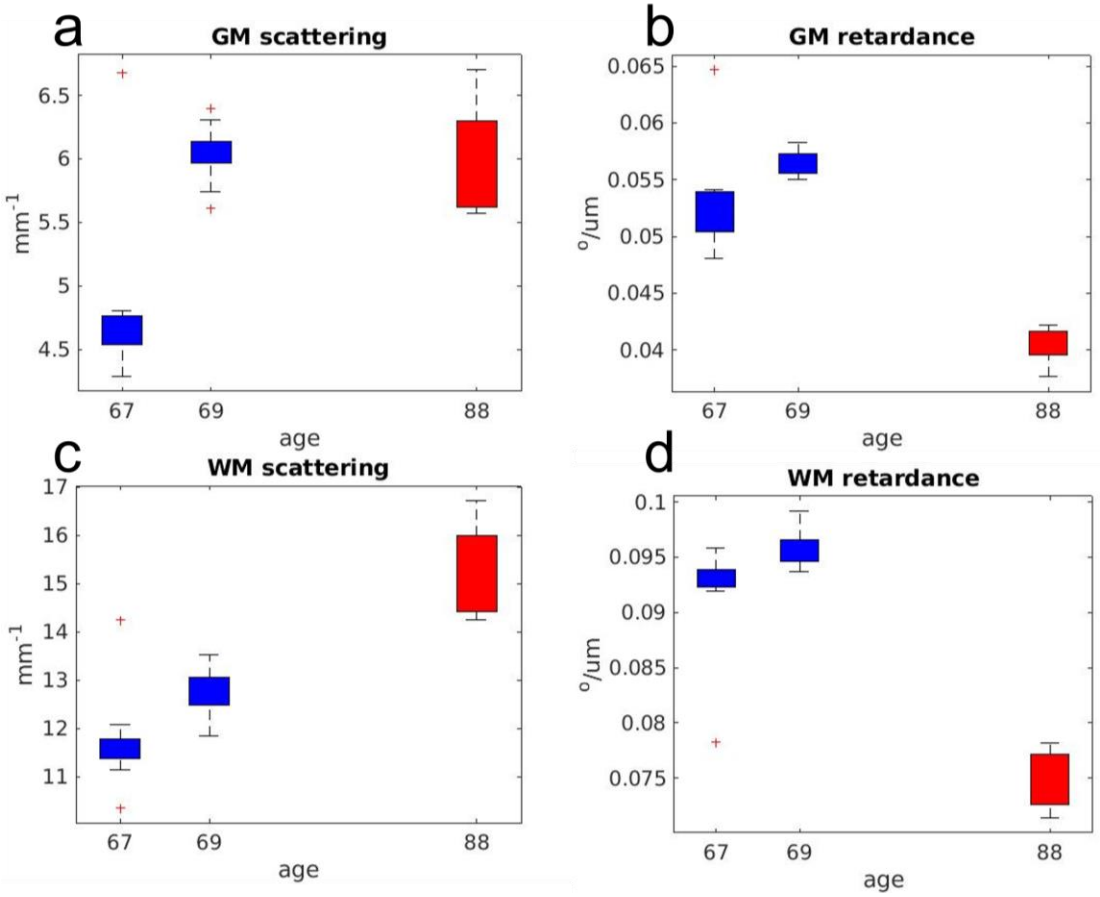

Figure 15 Measuring demyelination in aging brain using μ_s and retardance. Three samples that come from two age groups are used, one around 79 years old, the other from 88 years old. (a) Gray matter μ_s. (b) Gray matter retardance. (c) White matter μ_s. (d) White matter retardance.

3.8 Discussion

We have investigated the relationship of myelin density, cell density of human brain and scattering coefficient μ_s, back-scattering coefficient μ'_b as well as retardance and orientation measured with PSOCT. For the μ_s, we found myelin density is the major contributor to brain tissue scattering, and they share a strongly linear relationship. The slope of linear relationship is consistent across different regions of the human brain, which suggests a label-free measurement of myelin density using μ_s. Based on this finding, we developed a semi-supervised deep learning model that can transfer μ_s maps into virtual Gallyas stain images, which, after comparing with real Gallyas stain, are found to have vivid resemblance. The white-gray matter contrast of virtual Gallyas stain is indifferentiable from real Gallyas stain. In addition, virtual stain actually provides more contrasts across the white matter where there are more variation of myelin density, such as the first row in Figure 11. Besides, due to the complicated staining process of Gallyas silver stain, the stain results are prone to errors, which could display as the disappearance of cortical layers in second row of Figure 11 and over-stain or insufficient washing as seen in the third row of Figure 11. In virtual stain, however, these artifacts can be avoided due to the robust fitting algorithm of scattering coefficient and the accurate transferring mechanism of our deep learning network.

Currently, the resolution of our DS is limited to OCT resolution, which is about 12um lateral and 150um axial. As a result, we cannot provide sub-micron scale imaging of myelin sheath and axonal fibers as Gallyas stain does, which is usually imaged using a high NA

objective with sub-micron resolution. Srinivasan et al. has demonstrated Optical Coherence Microscopy using high NA objectives that achieved 0.9um lateral resolution [52] and revealed individual axons in mice brain. If using OCT images of that resolution for training the deep learning network, it is possible to see microscale structures in the virtual Gallyas stain images.

One of the limitations of the DS model is the stitching artifacts in the μ_s maps as well as in the virtual Gallyas stain, which appear as grid-like patterns. These stitching artifacts come from the nonuniformity of imaging setups across the FOV, including the intensity nonuniformity and focus nonuniformity, which can be improved by more careful correction of these parameters in the image and data processing steps.

Overall, our μ_s maps and virtual Gallyas stain derived from which proved to be useful in providing histology-level measurement of myelin content in human brain at mesoscopic resolution. As the whole process is fully automated, our method features much higher throughput, thus has the potential of providing quantitative measurements of myelin density over large scale and sample size.

While μ_s provides quantitative and robust measurement of myelin density, μ'_b and fitted retardance provide indicative contrasts about fiber structure, specifically, whether fibers are parallel or crossing each other. Both μ'_b and fitted retardance shows darken feature at the sub-sulcus white matter region, where the fibers are turning along the surface of cortex,

and multiple directions of fibers crossing each other. Comparing to μ'_b, retardance shows higher contrast of crossing fibers, especially after index matching the sample. Consequently, combining μ_s and retardance, PSOCT allows quantitative measurement of myelin density and organization across large area of human brain tissue.

We used high-resolution 2PM as microscopic corroboration of the mesoscopic measurement using PSOCT optical properties. We found that both birefringence and μ'_b highlighted the subcortical U-fibers (Figure 14.d), while μ_s was sensitive to myelin density in deep white matter (Figure 14.e). We used 2PM images to corroborate the above measurements. The highly organized U-fibers and densely packed fiber bundles of the deep white matter were recognized by the high resolution autofluorescence of 2PM. The different organizations of fibers in these areas might contribute to variation in these optical parameters. We demonstrated that by comparing the mesoscopic measurements from PSOCT with the microscopic information from 2PM, our system reliably measured human brain myeloarchitecture.

Neuronal cell body turns out to be a secondary contribution to the overall scattering, and the correlation varies across different brain regions. In somatosensory cortex we found a significantly positive correlation ($P<0.01$), indicating a strong laminar structure with differed neuron density and size, while in other brain regions we observed negative or moderately positive correlations. Indeed, most of the OCT studies on brain cancer samples have reported difficulties in differentiating cancer of various stages from normal grey

matter merely by scattering coefficient [53,54]. Our studies might provide an explanation for those challenges because cell body contribution is only a minor factor for light scattering in the brain. Further improvement of our scattering model may increase the sensitivity to neuron scattering.

We applied our quantitative methods to investigate the demyelination process in aging, and found increased scattering and reduced birefringence over two age groups. We have proposed an explanation for these changes based on myelin breakdown into defects that reduce birefringence, and brain atrophy that increase scattering. To give it more impacts more samples that cover a wider age range is necessary.

CHAPTER FOUR LABEL-FREE MEASUREMENT OF LIPOFUSCIN AND CELL SOMA OF POST-MORTEM HUMAN BRAIN

4.1 Introduction

Lipofuscin is an intracellular pigment that accumulates within neurons and other cells throughout the body as a result of normal cellular metabolism and aging[29]. It is often referred to as the "wear and tear" pigment due to its association with the accumulation of cellular waste products. Lipofuscin is commonly observed in neurons and is considered a marker of aging in the brain[55]. Its presence has also been linked to neurodegenerative disorders such as Alzheimer's disease[56,57].

Lipofuscin accumulates within the lysosomal compartment of neurons and other cells. Lysosomes are cellular organelles responsible for the degradation and recycling of cellular waste and damaged components. Over time, as the lysosomal degradation capacity declines with age, lipofuscin accumulates within these organelles, leading to its characteristic appearance as a granular material. The accumulation of lipofuscin is particularly prominent in long-lived postmitotic cells, such as neurons, which are unable to dilute or eliminate it through cell division.

One notable characteristic of lipofuscin is its autofluorescence property. When excited by light, lipofuscin emits fluorescence in the yellow-green to orange-red spectral range[58], making it easily detectable under fluorescence microscopy. This autofluorescence arises from the accumulation of fluorophores within lipofuscin granules, which include pigments

derived from oxidized lipids, protein aggregates, and advanced glycation end products. The autofluorescence nature of lipofuscin has allowed researchers to study its accumulation and distribution in cells and tissues, providing insights into its role in aging and neurodegeneration.

4.2 Samples

For the colocalization study of lipofuscin and neuron soma, a small human brain block was obtained from the Massachusetts General Hospital Autopsy Suite. The sample was obtained from a 53-year-old male's motor cortex that was neurologically normal without a previous diagnosis of neurological deficits. The sample handling procedure was the same as all other samples, The tissues were fixed by immersion in 10% formalin for at least two months [43]. The post-mortem interval did not exceed 24 h. 50 um slices were cut after block-face imaging for Nissl stain using the same procedure as in last chapter.

For the segmentation of lipofuscin and case comparison between Alzheimer's disease, Chronic Traumatic Encephalopathy (CTE) and normal control (NC), the 15 samples used in the digital Gallyas stain study in the last chapter were used.

4.3 Methods

4.3.1 Fluorescence life time imaging and sub-micron two photon imaging

Fluorescence life time imaging (FLIM) and sub-micron two photon imaging were carried out using a commercial Bruker Two Photon system. We used 20x water immersion objective with NA=0.6. Lateral resolution was 0.5um and axial resolution was 3um. Excitation was 820nm and the emission filter was 500–550nm. FLIM acquisition was using the Prairie View software and FLIM processing was using the SPCImage software, both are commercial software from Bruker Inc.

For comparing autofluorescence images to Nissl stain, as Nissl stain slice thickness was 50um, we did a depth scan in Bruker 2PM system with 10um step size, and merged 5 depths to match the Nissl slice thickness.

4.3.2 Segmentation of lipofuscin aggregates

Segmentation of lipofuscin was based on high-pass filtering of the image followed by adaptive thresholding. Specifically, the process was carried out in the following steps:

a) Low-pass filtering was applied on the 2PM long wavelength channel using the Gaussian smoothing function of ImageJ. We used Sigma (radius) value of 50, which corresponded to 100 μm. This empirical value was chosen to remove low frequency background variations but maintain high frequency details including the lipofuscin and tissue boundary.

b) The original image on the 2PM long wavelength channel was divided by the filtered image in (a). This way we normalize the low frequency background.

c) The resulting image from (b) was binarized using the Threshold function of ImageJ. We selected the Huang method for adaptive thresholding. We used the lower bound 1.4, which gave the best discrimination between lipofuscin and background. As the background was normalized in (b), the adaptive thresholding gives excellent discrimination of lipofuscin across the image, other than the tissue boundary as the signal was enhanced from the division in (b). Besides, the autofluorescence signal is stronger at the tissue boundary possibly due to the lower tissue surface, which results in a higher background and the thresholding missed lots of lipofuscin at the tissue boundary.

4.3.3 Statistical comparison of lipofuscin density across AD, CTE and NC

Statistical comparison of the three neurological cases were carried out in the IBM SPSS statistics software. Considering the small sample size (5 per each case), the distribution may not be gaussian. To consider that , we used two tailed mann whitney test that is more suitable for skewed distribution.

4.4 Using Fluorescence Life Time and Sub-Micron Resolution Two Photon Imaging to identify Lipofuscin in Autofluorescence Images

Lipofuscin can be identified in fluorescence microscopy by its bright and broadband emission spectra, which extend from 500nm to 700nm and even beyond[58]. And lipofuscin often appears as granular particles in brain tissue, which is different than other autofluorescence structures such as tube-like elastin and collagen. Lipofuscin can also be identified using the fluorescence life time microscopy (FLIM) due to its ~400 picosecond fluorescence lifetime[58], which is shorter than other autofluorescence particles. Figure 16.a shows a FLIM image taken in gray matter of human brain at 0.5um lateral resolution. The orange color, corresponding to a 300–400 picosecond fluorescence life time, and granule particles are lipofuscin. There are also green tube-like structures which is elastin-rich vessels. The background is green and blue-ish color, probably due to the elastin and collagen in the axonal fibers and extracellular matrix (ECM).

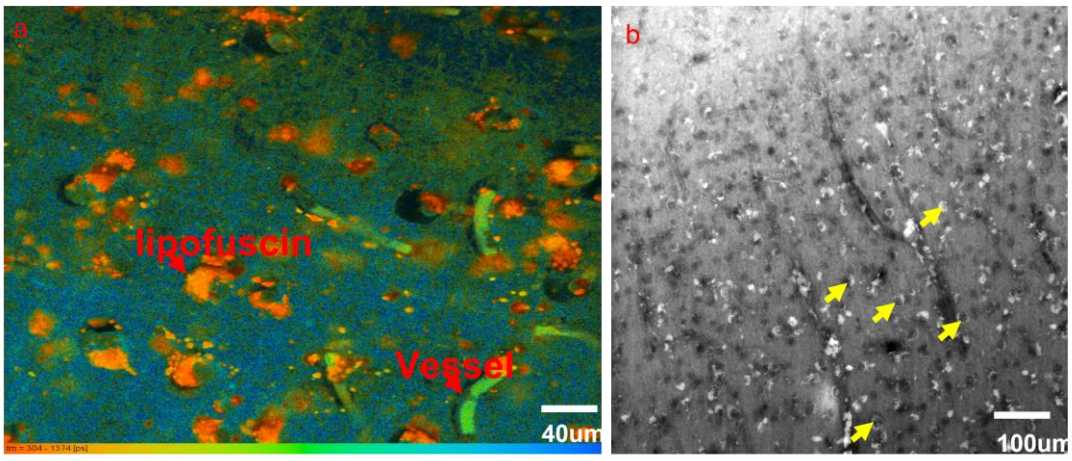

Figure 16 Identification of lipofuscin. (a) Fluorescence life time imaging (FLIM) of human brain tissue taken at gray matter region. Lipofuscin are the orange particles. Vessels and background appear as green to blue with longer fluorescence lifetime. (b) Intensity image of autofluorescence. Bright spots are lipofuscin, which often colocalize with mysterious dark spots. Blood vessels also appear as dark structures.

4.5 Colocalization of Lipofuscin and Cell Soma

In the FLIM images of Figure 16, we found lipofuscin is located within the margin of circular green-ish structures. As lipofuscin accumulates within the lysosomal compartment of neurons and other cells, we speculate the spatial distribution of lipofuscin should align with that of cell soma. Figure 16.b is a fluorescence intensity image of human gray matter region taken by a commercial two photon microscopy with 0.5um lateral resolution. Here we can see clearly the colocalization of lipofuscin with the circular dark spots as indicated by the yellow arrows. Lipofuscin is always at the perimeter of dark spots, but not all dark spots have lipofuscin, some smaller dark spots haven't developed lipofuscin. From these results, it is likely these dark spots are cell soma. To validate this, we sectioned a 50 μm slice after imaging with a Bruker 2PM and performed a Nissl stain on the same slice, which was a standard method for visualizing cell soma. We selected a region enclosing layers II, III and IV of cortex where a high density of neurons was expected and investigated neurons in three ROIs (Figure 17, a1–a3: Nissl; b1–b3: Bruker 2PM). We found the markers of lipofuscin and dark spots in the 2PM images agreed with the neurons in the Nissl stain at the same location (red and white arrows). Therefore, 2PM autofluorescence combining lipofuscin and dark spots can be used to quantitatively identify the neurons. Two observers counted the cell number in the Nissl stain and in the autofluorescence image (Figure 17, c1-c3). Both observers found similar counts of neurons in the Nissl and 2P images, and the correspondence rate between the two modalities was 92% on average.

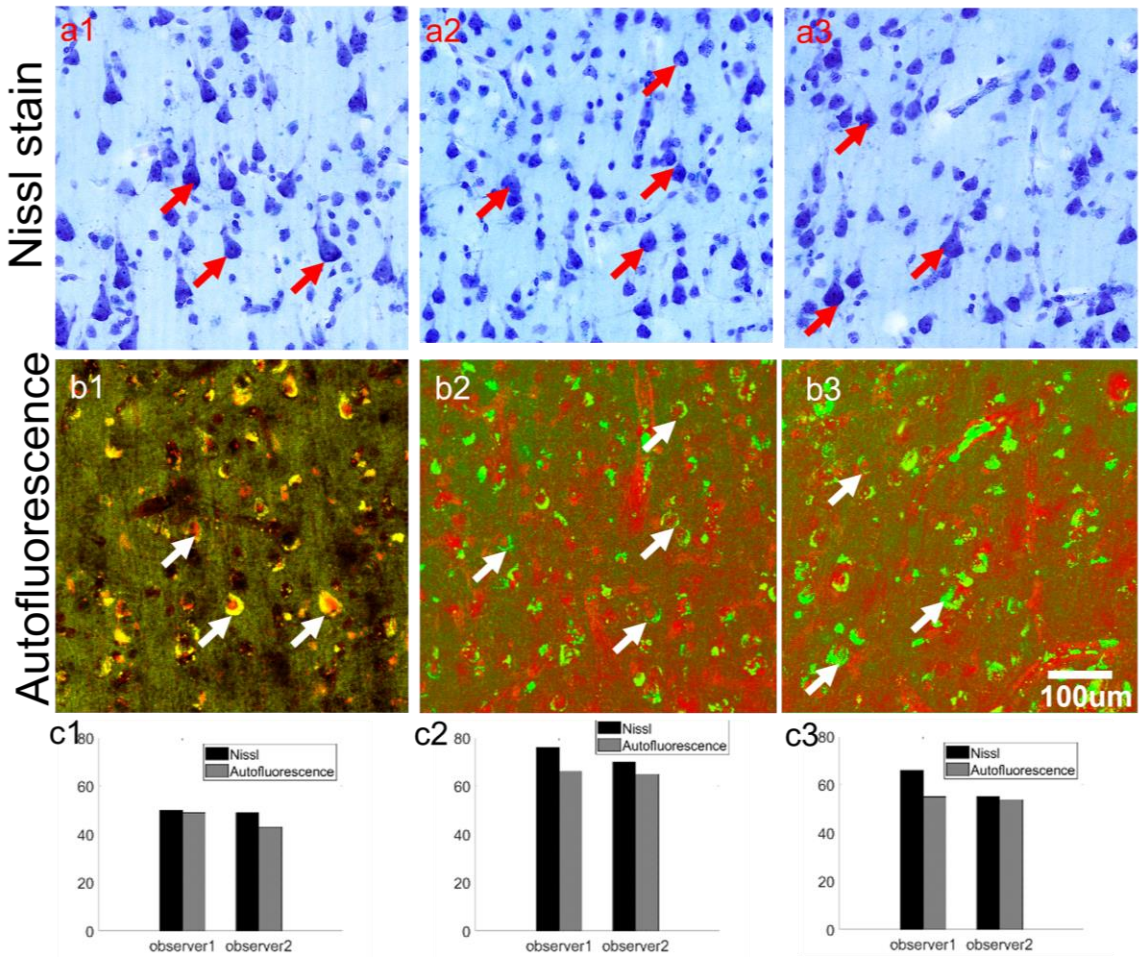

Figure 17 Autofluorescence images of brain tissue compared with Nissl stain. (a1–a3) Three ROIs in the Nissl stain image. ROIs were taken from the grey matter. (b1–b3) Bruker 2PM images of corresponding ROIs as in a1–a3, with lipofuscin in the green channel and inverted dark spots in the red channel. A few representative neurons in the Nissl stain and the corresponding dark-spot-lipofuscin structures are highlighted (red and white arrows). (c1–c3) Manual counts of neuron numbers from the two modalities by two observers.

4.6 Segmentation of Lipofuscin Reveals Its Spatial Distribution

Other than the colocalization with cell soma, lipofuscin itself has drawn increasing attention in the aging and degenerating human brain. The intraneuronal accumulation of lipofuscin is one of the most evident features in aged brain tissue[24], where the distribution in the cerebral cortex[61,62] and the role in neurodegeneration[55] is intriguing for in-depth

investigation. Figure 18.a shows the autofluorescence image from a 2x2cm^2 brain sample using the long wavelength channel of our 2PM, which was dominated by lipofuscin autofluorescence. The grey matter was brighter than the white matter, which may be due to the higher density of lipofuscin in grey matter. Figure 18.b-c shows the zoom-in of the left red box around the crown of the cortex and the segmented lipofuscin particles. We found densely distributed lipofuscin across the whole area (Figure 18.b), especially some larger lipofuscin particles as indicated by the red arrows. After segmentation, the large lipofuscin particles were easier to recognize. The lipofuscin in the superficial layer was sparsely distributed while in deeper layers small lipofuscin particles were densely distributed. In Figure 18.d-e, we show the lipofuscin distribution around the sulcus region in the right box of (Figure 18.a). Lipofuscin was densely scattered in all cortical layers (Figure 18.d). While examining the segmentation map (Figure 18.e), however, we also found layer structures enclosing different densities and sizes of lipofuscin within the grey matter, as indicated by the red arrows. It is noticeable that the background intensity of autofluorescence was inhomogeneous. Strong background autofluorescence reduced the contrast of lipofuscin and could cause error in the segmentation. For example, an empty hole (yellow arrow) was found in Figure 5.c.

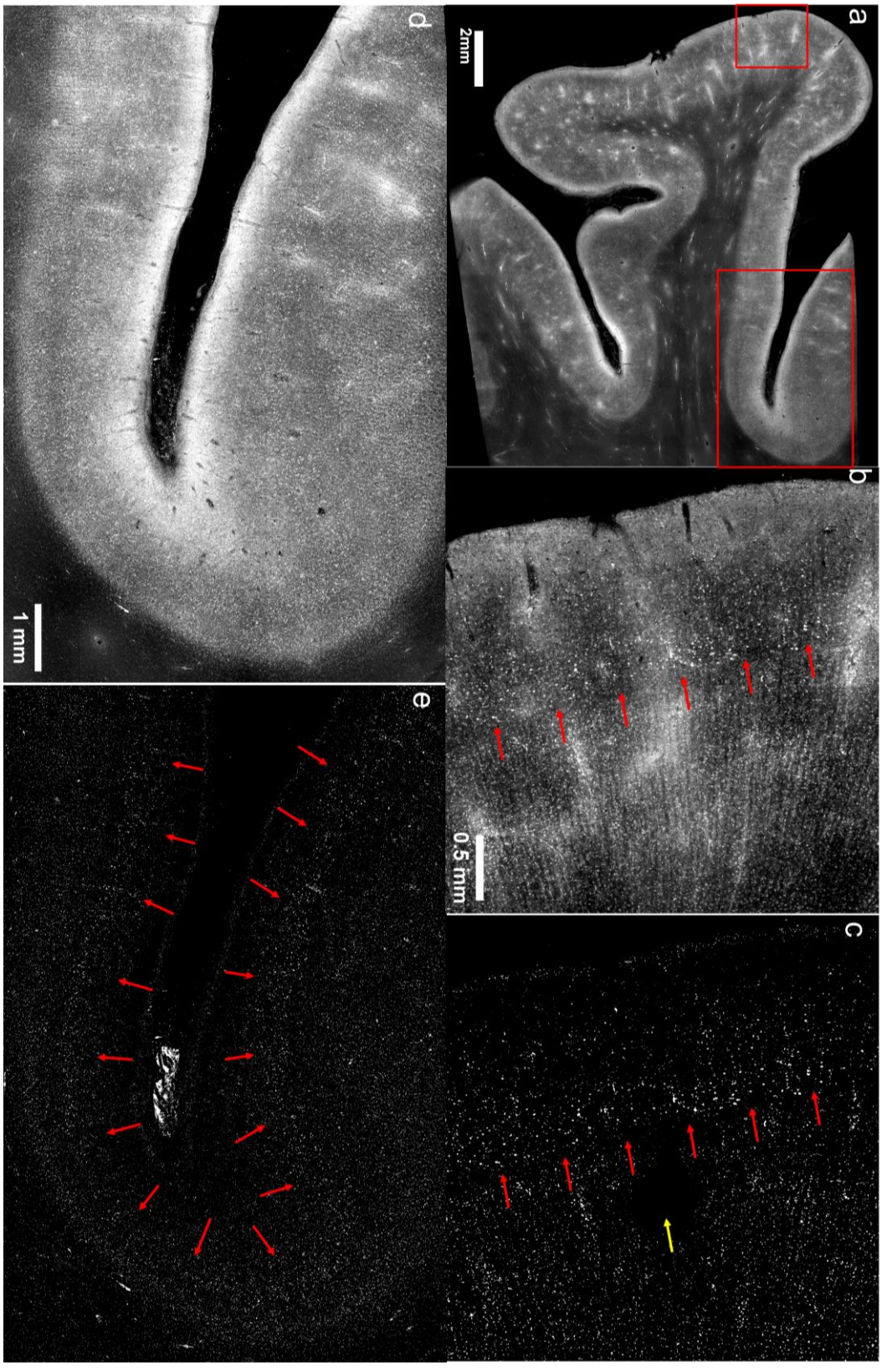
a
2mm
b
0.5 mm
c
d
1 mm
e

Figure 18 Autofluorescence image of lipofuscin from a brain sample and the segmentation of individual lipofuscin particles. (a) Overall intensity map of autofluorescence from a slice. (b) zoom into the left red box in (a) to show the lipofuscin distribution at the crown of cortex. Some larger lipofuscin particles form a layer in the grey matter and are pointed by the red arrows. (c) segmentation of the lipofuscin particles in (b). The larger lipofuscin particles were better visualized. An empty space is pointed out by the yellow arrow. (d) zoom into the right box in (a) to show the lipofuscin distribution around the sulcus of cortex. (e) Segmentation of the lipofuscin in (d). A dense lipofuscin layer was indicated by the red arrows.

4.7 Quantitative Lipofuscin Density and Distribution In Neurodegenerative Diseases

With the segmented lipofuscin particles, a few quantitative metrics are possible to calculate for evaluating the spatial distribution of lipofuscin, including the mean radius map of lipofuscin, the number density map, and the product of these two quantities, which we name as the density map. Examples from one of the 15 samples are given in Figure 19 first row, from left to right is the mean radius, number density, and the density map, which is the product of the two previous quantities.

The radius map clearly reveals a layer in the gray matter with larger lipofuscin size (indicated by the red arrows), which corresponds to the layer structure we saw in Figure 18.e. This layer is clear in all 15 samples we imaged, suggesting it may relate to a common structure in the cortex, probably the cortical layer II and III where there are larger pyramidal neurons. The number density map highlights the whole grey matter, suggesting the gray matter has much denser lipofuscin population comparing to white matter. Within the gray matter there are also variations of lipofuscin density, and some region appears to have more lipofuscin, as highlighted by the red arrow. The density map is essentially a product of radius and number density maps as it shows the total amount of lipofuscin across the whole

sample. In this sample the density map vaguely shows two higher density lipofuscin layers in the gray matter as indicated by the black arrows. Comparing to the lipofuscin segmentation image in Figure 18.e, these two layers may correspond to the layer II and III with larger lipofuscin particles, and infra layers with smaller but denser lipofuscins, respectively. It also highlights the gray matter region that has more lipofuscin density as in the number density map, but with slightly higher contrast (red arrow). Besides, the vessels in the white matter are also brighter, similar to the radius map but with clearer background. In regions with bright vessels that saturate the image, segmentation does not turn out well and leaves an empty hole, these regions are visible in all three maps (green arrows).

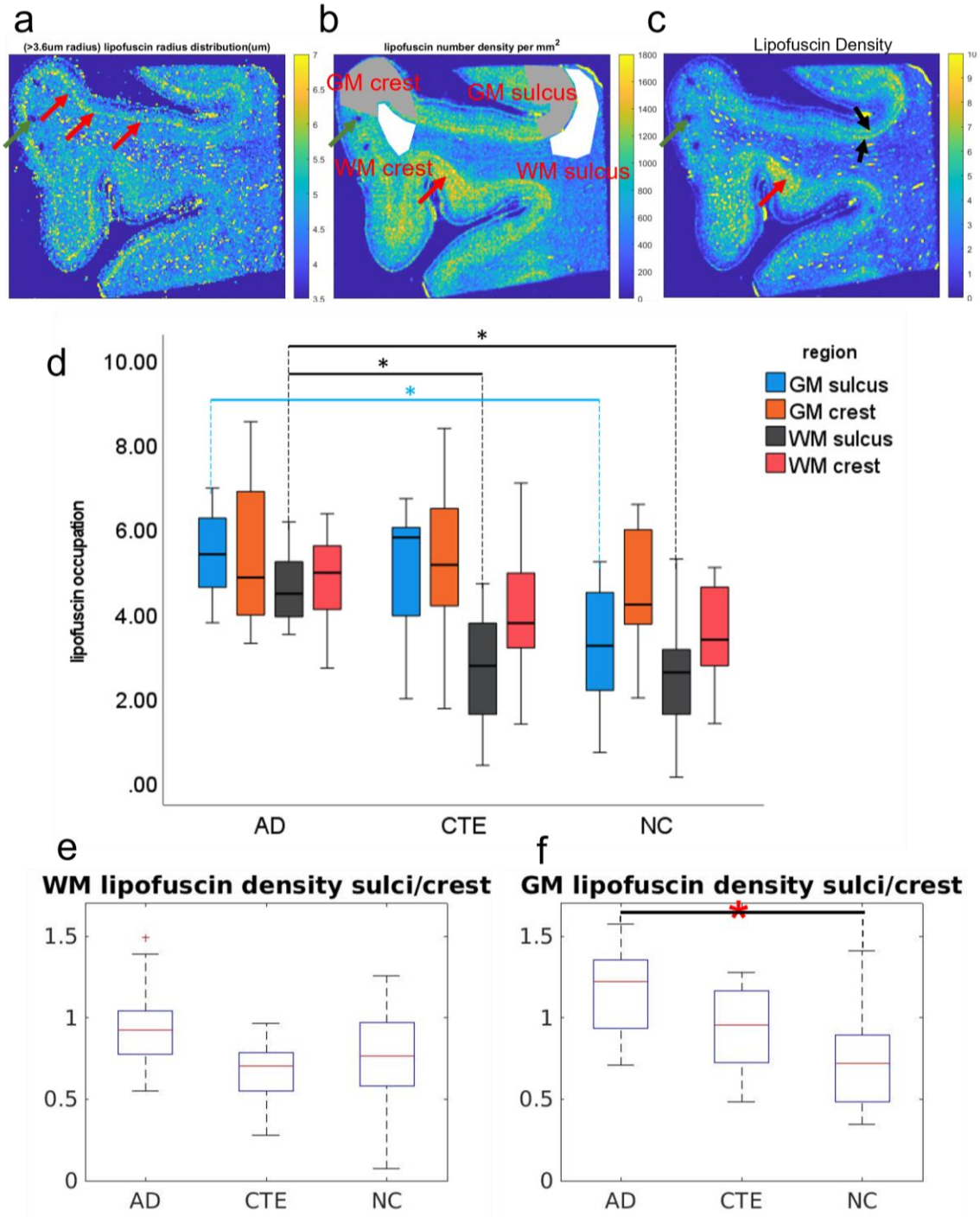

Figure 19 Quantitative measurement of lipofuscin radius map (a), number density map (b) and density map (c). First row shows the three different metrics for one of 15 samples. The gray and white masks in (b) are example ROIs used to calculate the mean value of density map. (d) statistical comparison of the gray matter sulcus, gray matter crest, white matter sulcus, white matter crest among the AD, CTE and NC cases. (e–f) statistical comparsion of the sulcus to crest ratio of lipofuscin density among AD, CTE and NC.

With these quantitative metrics, we can compare the statistical differences among AD, CTE and NC cases in terms of lipofuscin distribution. As the density map incorporates both lipofuscin size and number density, we choose it to start with. We manually selected ROIs in the crest of gray and white matter, and the sulcus of gray and white matter of each image (Figure 19.b), 10 images per sample. Using these ROIs, we calculated the average lipofuscin occupation in the crest of GM, crest of WM, sulcus of GM, sulcus of WM for AD, CTE, and NC cases, each case has 50 sample points (5 samples multiply 10 slices per sample). Figure 19.d shows the comparison between AD, CTE and NC cases for these four regions. We found the difference is significant for the GM sulcus between AD and NC, with the mean value of AD GM sulcus 60% higher than that of NC GM sulcus. For the WM sulcus, AD case is significantly higher than both NC and CTE, both higher by 50%. For the crest of both white and gray matter, no significant differences are found between any cases. From these results, we can draw a few conclusions. First, AD brain has more lipofuscin than CTE and NC brain at old age (70–90 years old), indicating that the AD pathology is correlated with the lipofuscin formation. CTE, however, doesn't show significant increase of lipofuscin in any regions, suggesting that CTE pathology does not affect the lipofuscin formation. Second, the increase of lipofuscin in AD is mostly in the sulcus region in both white and gray matter, the lipofuscin density in the crest region is comparable to NC. Considering the unchanged crest, we can use it as normalization factor, since different acquisition may have slight change in microscopy configurations that affect the results. Figure 19.e–f show the ratio of sulcus over crest for white and gray matter, respectively. This normalized quantity should remove the image setting bias and depend only on

pathology. Here we found that both WM and GM ratio in AD is still higher than CTE and NC, while GM still has statistical significance, which agrees with previous findings that AD has slightly more lipofuscin[57] than the other two cases and this increase of lipofuscin is mostly in the gray matter sulcus, and slightly on the white matter sulcus. Specifically, we found that in gray matter, the ratio in AD is mostly above 1, while NC is mostly below 1. This means in normal brain crest has more lipofuscin, while in AD brain lipofuscin in crest is not changing much, but lipofuscin in sulcus surpassed crest. This indicates the gray matter sulcus is more vulnerable to AD pathology with regard to the accumulation of lipofuscin. The ratio of CTE, while also being higher than NC, does not appear to have statistical significance.

We also investigated the three lipofuscin metrics in the white and gray matter during aging process. Figure 20 shows the results from 5 normal control samples that covers from 64 and 88 years old. In terms of the area fraction, we found both white and gray matter have increased lipofuscin linearly. The white matter started with less lipofuscin area fraction, but increases faster than GM. At around 88 years old, they have about the same level of area fraction. For the number density, both white and gray matter have increased lipofuscin numbers, they started at about same number, but at the old age, surprisingly, white matter has more numbers of lipofuscin than gray matter. For the lipofuscin size, in GM the size remained relatively unchanged, but in white matter lipofuscin grows larger. There's one outlier at about 67 years old that with much larger size, which was biased from bright vessels that were mistaken as lipofuscin.

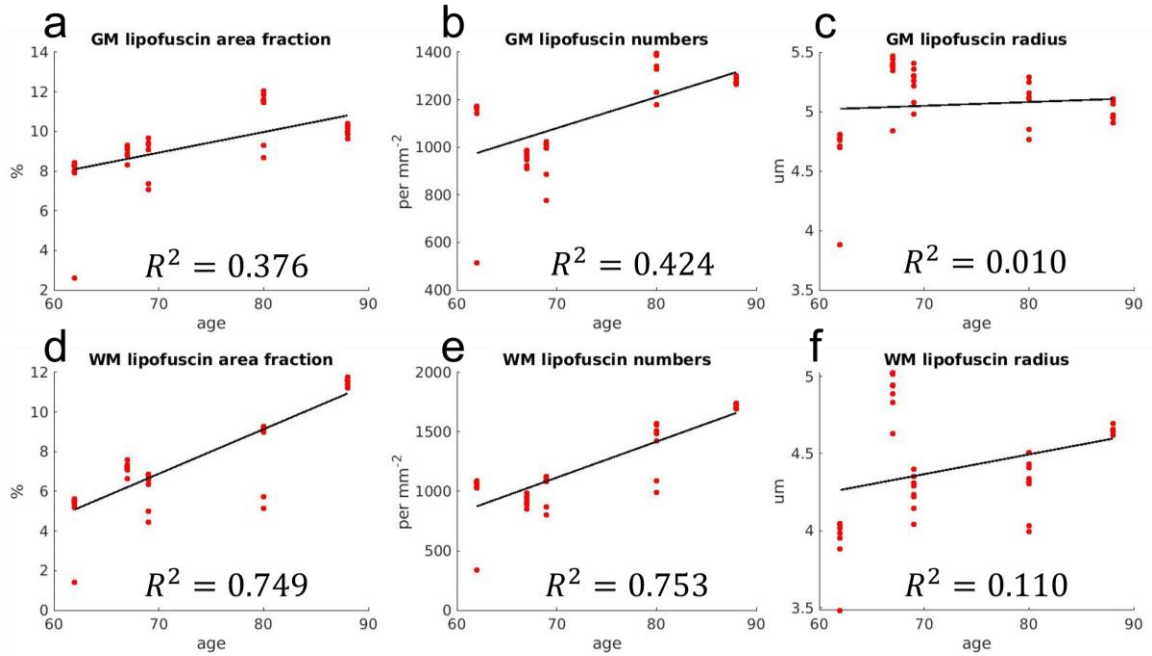

Figure 20. Measurements of lipofuscin area fraction, number density, and size in white and gray matter in the aging process. (a-c) lipofuscin quantification in the gray matter, from left to right, area fraction, number density, and mean radius. (d-f) lipofuscin quantification in the white matter.

4.8 Discussion

We have demonstrated the label-free large-scale imaging of lipofuscin aggregates in human brain tissue using the two photon autofluorescence microscope of our hybrid system and validated the results using FLIM as well as sub-micron resolution 2P imaging. Lipofuscin is found to colocalize with cell soma, due to the fact that lipofuscin is generated mostly in the lysosomal of cell body. Besides, we found another feature that can be used to indicate cell soma, the lack of autofluorescence of soma comparing to ECM. By combining the lipofuscin particle with dark-spot appearance of cell soma, we proposed a label-free method of identifying and counting cells, especially for large neurons in brain tissue.

Comparing to the Nissl stain, which is a gold standard method for visualizing cells, our method achieved 92% accuracy at submicron resolution. Currently, we are using 0.5um resolution autofluorescence images for the cell counting, which is 8 times higher than that of our home-built 2PM. Fortunately, recent advancements in machine learning methods show promise as a mean of segmenting low-resolution images using prior knowledge from high-resolution ones[64,65]. Besides, there's a 2X resolution increase in our system as we are currently down-sampling to speed up 2PM imaging with PSOCT. For small sample blocks that we do not care about extending imaging time, we can sample 2PM at the Nyquist, which will give about 2.4um resolution, which will definitely help the imaging and identifying of lipofuscin and cells.

We also developed segmentation of lipofuscin aggregates, from which we calculated three quantitative measurement of lipofuscin spatial distribution, the radius map, number density map, and area fraction map. From these maps we discovered that lipofuscin forms some layer structures in the cortical gray matter with slightly larger size (Figure 19.a), which may relate to the pyramidal neuron distribution in cortical regions. We also found regional abundancy of lipofuscin in some sulcus region (Figure 19.b-c), the underlying mechanism worth more in-depth investigation, we discuss it more in the Chapter 5.4. We applied the quantitative measurements of lipofuscin to neurodegenerative processes and aging. We found significant more lipofuscin in the white and gray matter sulcus, comparing to normal control samples. And by comparing the sulcus to crest ratio, we found in AD and CTE, lipofuscin are tend to be more located at sulcus, while in normal control, lipofuscin are

most abundant in the crest. These results indicate that lipofuscin, being an aging pigment, is also involved in the neurodegenerative processes. In the aging process, we found lipofuscin increases as aging, which is in agreement with literature. But in addition to that, we were able to carry out more in-depth analysis of the size and number density in white and gray matter separately. We found both white and gray matter have increased lipofuscin numbers, but the size of lipofuscin is remained in gray matter throughout this age range, but in white matter the size of lipofuscin still increases. Our hypothesis is that since white matter has more myelin, and thus more myelin degeneration, the cells that in charge of myelin recovery has more stress in white matter, hence more lipofuscin accumulation, especially in the later age. In the early age, the neurons and cells in gray matter are more involved in the brain activity, thus started accumulating lipofuscin earlier, and saturate earlier, resulting in the unchanged lipofuscin size.

CHAPTER FIVE APPLICATIONS AND CONCLUSIONS

5.1 Investigating the Demyelination Process in Neurodegenerative Diseases

5.1.1 Introduction

Demyelination is a critical pathological feature observed in various neurodegenerative diseases, including Alzheimer's disease (AD) and chronic traumatic encephalopathy (CTE). Myelin, a fatty substance surrounding nerve fibers in the central nervous system (CNS), plays a vital role in facilitating efficient neuronal communication. The disruption or loss of myelin, known as demyelination, severely impairs neural transmission and contributes to the progression of these debilitating neurodegenerative disorders.

In AD, a neurodegenerative disorder characterized by progressive cognitive decline and memory loss, demyelination has been observed in affected brain regions[67–69]. Although AD primarily affects regions crucial for memory formation, such as the hippocampus and cerebral cortex, myelin loss extends beyond these areas. Studies have shown that myelin breakdown occurs in white matter tracts throughout the brain, impairing long-range connectivity between different brain regions[68]. Demyelination in AD may contribute to cognitive dysfunction and disrupt the synchronized communication necessary for normal brain function.

CTE is a neurodegenerative disease associated with repeated head injuries, particularly in individuals engaged in contact sports or military service. The hallmark feature of CTE is

the deposition of abnormal protein aggregates, including tau, throughout the brain. Alongside tau pathology, demyelination has been observed in CTE cases, primarily in regions affected by repeated traumatic injury[70,71]. The accumulation of tau and other pathogenic factors appears to trigger inflammation and disrupt myelin integrity, leading to widespread demyelination. Demyelination in CTE may contribute to cognitive impairment, behavioral changes, and other neurological symptoms observed in affected individuals.

Traditionally, myelin content can be imaged using histology methods such as Gallyas Silver stain. Quantitative measurement of myelin density can be derived from histology images by calculating the optical density value (OD). However, these methods are laborious processes that are prone to human error and are inevitable from tissue loss and distortion, making it challenging for volumetric applications. MRI contrasts has been shown to show correlation with myelin density in human brain. Stüber et al.[72] investigated the quantitative correlation between myelin content and T1 and T2 contrasts of MRI along with the iron concentration and found strong linear correlation (r=0.933 for multi-variate linear regression). However, the spatial resolution of MRI is limited to a few hundred microns to mms, from which resolving small structures such as the thin layer structures in gray matter and local variations of myelin density can be challenging. Our approach, however, provides mesoscopic, distortion-free and quantitative measurement of myelin content at tens of cubic centimeters scale. We have demonstrated that the three optical properties, μ_s, μ'_b and retardance provide complementary information about myelin density and structure. Besides, we also show that 2PM can be used to provide microscopic

validation of the mesoscopic PSOCT measurements of myelin content using the autofluorescence of axonal fibers. Consequently, our hybrid system has great potential to study the microscopic to mesoscopic, large scale and volumetric myelin content of post-mortem human brain, which is beneficial for delineating the role of demyelination in neurodegenerative diseases such as AD and CTE.

5.1.2 Future Steps

We are currently applying this method to the 15 brain samples obtained from Boston University Alzheimer's Disease Research Center and CTE Center and investigating the difference in scattering coefficient and birefringence between AD and CTE with NC. We hypothesize that the optical tissue properties measured with PSOCT change due to myelin fragmentation in diseased cases. In normal control cases, myelin is predominantly intact while in diseased cases, the scattering coefficient μ_s might increase as a result of the tissue having more small structure myelin defects. Meanwhile, as the anisotropic structure of myelin sheath transition to less organized structure during the formation of myelin defects, the birefringence property of brain tissue may drop, and likely results in a decreased retardance measurement. By exploring the demyelination aspect of neurodegeneration, we are trying to bring attention to the study of myelin degradation in AD and CTE, which is believed by some researchers that myelin degradation happens in the early stages of AD.

5.2 Investigating Vasculature Disease And Abnormalities

5.2.1 Introduction

The brain's vasculature consists of a complex system of arteries, arterioles, capillaries, venules, and veins. Arteries carry oxygenated blood from the heart to the brain, while veins return deoxygenated blood back to the heart. The network of capillaries connects the arterial and venous systems and allows for the exchange of gases, nutrients, and waste products with the surrounding brain tissue.

Changes in vascular morphology have been found in the post-mortem brain tissue using standard histology and optical microscopy. For example, increased tortuosity has been observed in the white matter vessels that are downstream of the penetrating arterioles as early as in middle age (around 55 years old)[73,74]. It is also reported that there is an increase in spiraling and looped vessels in several areas of the brain in AD[75]. Several studies also suggest decreased capillary density in older human brains[76,77].

Mapping the vasculature of the human brain and measuring the vascular pathology is crucial for understanding the aging and neurodegenerative diseases such as AD and CTE. Traditionally, vasculature has been studied using histology methods on thin brain slices[78,79]. Similarly, all the shortcomings of histology including laborious processes, tissue loss and distortion apply here as well. Recently, several research groups used serial sectioning OCT to evaluate 3D vascular structures and have produced promising results of

measuring vascular morphology and density across large volumes of brain tissue. Yang et al.[80] developed vessel segmentation algorithm of OCT volume based on a tubeness filter and quantitatively evaluated the tortuosity, density and length distribution of vasculature. However, due to resolution limit and speckle noise, the resolvable vessel size is limited to around 20um, insufficient to visualize small vessels and capillaries, which most vascular disease studies[81,82] are interested in.

Multiple components of vessels and capillaries are two-photon excitable, such as the collagen, elastin[27], and iron-free variants of hemoglobin. The presence of these endogenous fluorophores in postmortem human brain offers opportunities for label-free, high-resolution imaging of small vessels and capillaries using autofluorescence 2PM, which can complement the images provided by PSOCT.

5.2.2 Sample

An early stage CTE brain sample (CTE stage II, 26-year-old male, Dorsal Lateral Frontal) was used to image the vasculature using both PSOCT and 2PM. The sample handling procedure was the same as all other samples, The tissues were fixed by immersion in 10% formalin for at least two months. The post-mortem interval did not exceed 24 h.

5.2.3 Results

Figure 21 shows the comparison of vessels imaged by PSOCT and 2PM. In PSOCT, only the large vessels are visible and they are sparsely scattered across the image. In 2PM,

however, many more vessels emerge as bright structures in both white matter and gray matter. Much smaller vessels and even capillaries are captured in the autofluorescence image, the diameter of the smallest visible vessel in the gray and white matter are 6um and 10um, respectively.

The strong autofluorescence may come from the residual red blood cells within the vessels as the hemoglobin is autofluorescent. In animal studies using mice and monkey brains, the brain is often perfused to remove blood to reduce the autofluorescent background. In human brain study, perfusion is unethical and not allowed, which, given the hardship of staining large block of human brains, is actually beneficial as the blood provides a useful marker for the blood vessels.

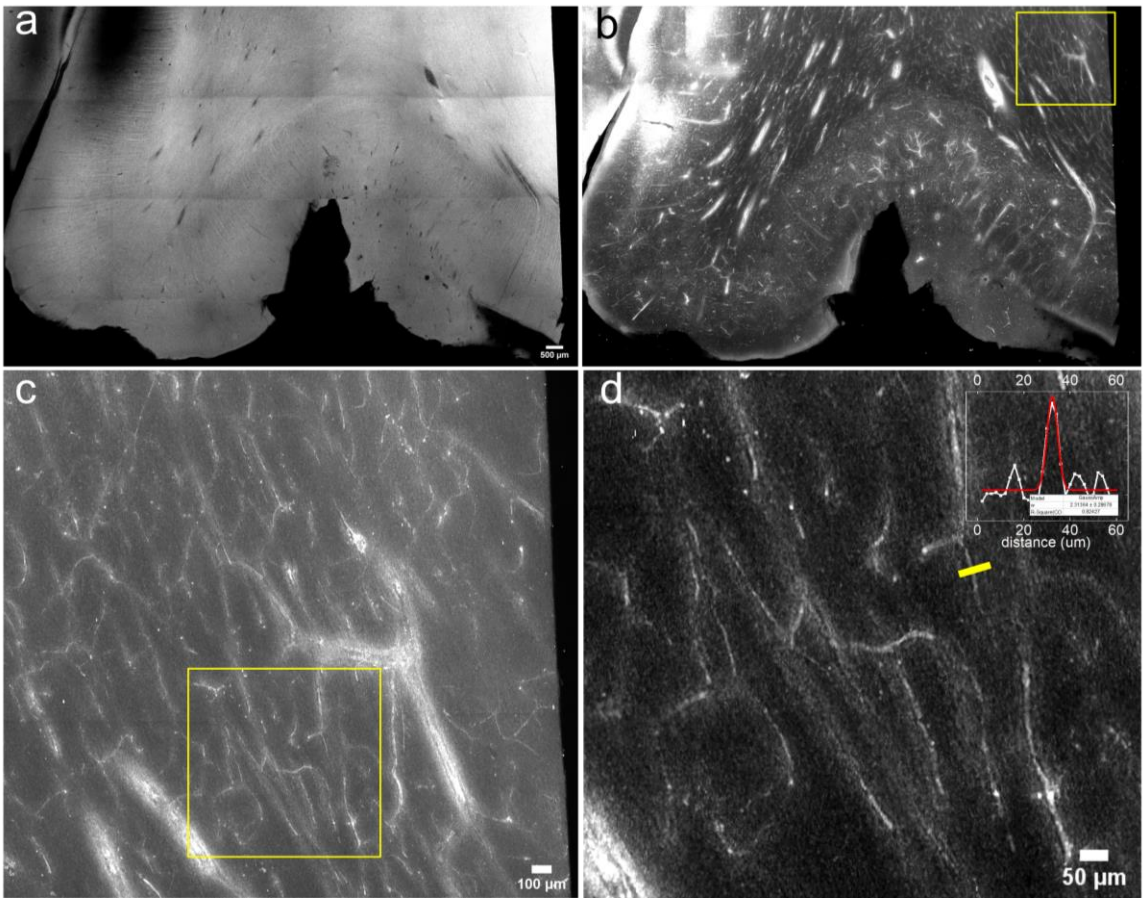

Figure 21 Comparison of PSOCT and 2PM imaging of vasculature. (a) OCT image of 150um depth. (b) 2PM image MIP of the same 150um depth. (c–d) zoom in to the ROI showing the intricate structure of vessels. Inset shows the diameter of the small vessel is 10um.

5.2.4 Discussion

During the imaging of this sample, the lateral pixel size is 2um, resulting in a down-sampled 4um theoretical resolution, larger than the 2.4um optical resolution. At such resolution, segmenting the less-than 10um capillaries might be challenging. Again, we are down-sampling 2PM to catch up with the imaging speed of PSOCT, so that the imaging of several tens of cubic centimeter of brain tissue can finish in a reasonable time. However, for small sample size that would take only a half day to image, increasing the resolution

and extending the imaging time to a few days is acceptable, but the higher resolution will make it easier to image and segment small vessels and capillaries, which would be extremely useful to quantitatively measure the vasculature in human brain. Additionally, we skipped two thirds of the brain tissue in depth for the same reason. If we perform depth scan to cover the whole tissue for 2PM, it will enable us to image the whole vasculature at microscopic resolution. Consequently, one of the future steps is to image brain tissue at higher resolution with depth scanning to cover the whole sample for complete vasculature mapping.

For the vessel segmentation algorithm, other than segmenting vessels in 3D as in PSOCT, here we only need to segment them in 2D images and stack the segmentation to form 3D vasculature. The tubeness filter used in Yang et al.[80] paper could apply here with minor modification, or other segmentation methods could be useful as well[83]. The axial pixel size will be 50um, corresponding to the 2PM depth of focus, which is sufficient for calculating metrics such as vessel density, and vessel tortuosity for the in-plane vessels. This way, it can enable the investigation of small vessel and capillary abnormalities in AD and CTE, which is challenging to achieve in OCT images.

5.3 Counting Cells in Post-Mortem Human Brain for Cell Death Study in Neurodegeneration

Neurons are the fundamental building blocks of the nervous system and are responsible for transmitting and processing information in the form of electrical signals. The human brain

contains billions of neurons, forming a highly complex and interconnected network. During neurodegenerative processes, such as Alzheimer's disease (AD), Parkinson's disease, or Huntington's disease, neurons can undergo degeneration and death[84–88]. This neuronal loss is a characteristic feature of these disorders and contributes to the progressive decline in cognitive or motor functions associated with them. In AD, for example, the loss of neurons is observed particularly in brain regions important for memory and cognitive functions, such as the hippocampus[89]. Being able to accurately image and count the neuron density along the progress of disease state is essential to help understand the mechanism of these neurodegenerative processes. Currently, imaging cells including neurons in the animal brain is relied on immunohistochemistry (IHC) such as Nissl stain and DAPI stain, the result of which is limited to the penetration of antibodies using in IHC. Staining of large volumes of human brain is challenging with most antibodies and staining procedures used nowadays.

In our work, we explored the intrinsic contrasts that can be used to image cells in post-mortem human brain, which includes the aging related lipofuscin aggregates and the dark appearance of cell soma. Combining these two contrasts, we have demonstrated identifying and counting more than 92% cells in one block-face imaging at 0.5um resolution as compared to Nissl stain. However, there’s still a 4-8 times resolution difference between the trial and our home-built 2PM. By sampling at 1um step size, we can increase our current 4um resolution to about 2.4 theoretical optical resolution. To bridge the resolution barrier, recent advancements in machine learning methods show promise as a means of segmenting

low-resolution images using prior knowledge from high-resolution ones[64,65].

Hippocampus turns out to be an interesting region as the scattering coefficient map shows clear contrast of cells in the CA1–CA4 region as shown in Figure 12. Resolving the cells in cerebral cortex using OCT has been shown if imaged at microscale resolution[90]. For the scattering coefficient, however, due to the resolution limit as well as the down-sampling step during the fitting process, it cannot see any cellular level structures in cerebral cortex. But hippocampus seems to be an outlier. Besides, hippocampus is the most important region of cell death study in AD[91]. Consequently, imaging hippocampus using the scattering coefficient combined with microscale 2PM would be super interesting in terms of measuring cell density and cell death for a longitudinal study of disease development.

5.4 Investigate the Spatial Relationship of Lipofuscin and Neurofibrillary Tangles

Neurofibrillary tangles (NFTs) are abnormal structures that are associated with AD and CTE, and are one of the hallmark features of these conditions and play a crucial role in their pathogenesis[92,93]. NFTs are primarily composed of an abnormal protein called tau. Tau is a microtubule-associated protein that helps stabilize the structure of nerve cells and aids in the transportation of nutrients and other essential molecules within the cell. However, in AD and CTE, tau undergoes pathological changes and becomes hyperphosphorylated, leading to its aggregation into paired helical filaments. These filaments then form NFTs, which accumulate inside neurons, particularly in regions of the brain involved in memory and cognitive functions.

In both AD and CTE, the severity and distribution of NFTs correlate with the degree of cognitive impairment and neurodegeneration. Understanding the role of NFTs in AD and CTE is crucial for advancing our knowledge of these diseases and developing potential therapeutic interventions. Currently, NFT is visualized using histology methods[94]. Similar to all histology methods, staining of NFT is also laborious and suffer from inevitable tissue loss and distortion.

Lipofuscin may be potential markers of distribution of NFT through their relationship with a specific ECM structure, the perineuronal nets (PN). Morawski et al.[66] compared the spatial distribution of lipofuscin and PN, an ECM component that protects the neurons from oxidative stress, and found inverse relationship between these two structures. Cells with rich PN shows absence of lipofuscin, while cells that lack PN enclosures more lipofuscin. Besides, Bruckner et al.[56] compared the spatial pattern of PN and neurofibrillary tangles (NFT), and also find inverse relationship, i.e., regions with abundant PN are less affected by neurofibrillary tangles. Based on these studies, we believe the spatial distribution of lipofuscin and NFT share similar spatial pattern. In other words, measuring lipofuscin distribution across cortical layers could give label-free estimation of NFT distribution. Such method could be useful in investigating the neurodegenerative diseases including AD and CTE.

5.5 Conclusions

We have developed a hybrid system that combines serial sectioning PSOCT and 2PM, and demonstrated the imaging and reconstruction of large volumes of post-mortem human brain tissue. PSOCT achieves 5um isotropic resolution over 150um of depth of focus with 95dB SNR on both polarization channels and negligible sensitivity roll-off. 2PM achieves 2.4um and 48um lateral and axial resolution, which was down-sampled to be 4um resolution for imaging faster. The 3x3mm^2 FOV of both PSOCT and 2PM reduced the imaging down-time during stage translation between tiles and improved the throughput. We pre-calibrated the XYZ dimensions of imaging distortion and developed distortion correction routines for correcting both geometric and intensity distortions for better image quality. With the distortion correction and because the two microscopes imaged the same sample simultaneously with largely overlapped FOV, the need for image registration between PSOCT and 2PM in post-processing was markedly reduced. For the serial sectioning, we utilized a custom vibratome with 2.5inch sapphire blade that enables unprecedent large brain block sectioning. We optimized the cutting parameters for optimal cutting flatness and found a larger than 1mm peak to peak amplitude of blade oscillation is pivotal for cutting non-homogeneous tissue such as brain. For the reconstruction, we developed an automated workflow in MATLAB that will produce the 2D and 3D reconstruction of POSCT and 2PM images for further analysis.

Although previous studies have combined OCT with 2PM to enrich the image contrasts of the individual modalities[24,30,31], one of the challenges of combining PSOCT with 2PM is

system birefringence that prevents accurate measurement of sample retardance and orientation. System birefringence originates from the optical telescopes, dichroic mirrors, and scanning mirrors, and results in a substantial bias to the polarization measurements of the sample. We removed this bias by using an adjustable retarder that enabled measuring true retardance and orientation from the sample. As a result, we were able to investigate multiple signals of scattering, birefringence, and autofluorescence from the human brain at different scales. Utilizing these contrasts, we enrichened the measurements of the myelin content, vascular structure, lipofuscin, and neurons in volumetric brain tissue blocks.

For myelin content, we estimated μ_s, μ'_b and retardance from PSOCT for investigation of myelin density and used high-resolution 2PM as microscopic corroboration. We have quantitatively investigated the different contributions to μ_s from myelin content and cell scattering in human brain samples. We have found that the scattering coefficient is strongly correlated with the myelin content ($P < 10\text{-}10$, $PCC > 0.85$) and that linear relationship is retained across different regions of the brain. The results suggest that μ_s can be used as a robust predictor for myelin density of the human brain. Cell body, however, turns out to be a secondary contribution to the overall scattering, and the correlation varies across different brain regions. Based on the strong relationship between μ_s and myelin density, we developed a deep learning model that transfer μ_s map into virtual Gallyas staining that will facilitate the measurement of myelin content for neuroanatomy and neurodegenerative studies. The results from our deep learning model show as good quality as real Gallyas stain, sometimes even better at visualizing the cortical myelin layers and white matter fine

structures (Figure 11). The application of this method to hippocampus provides supervising results as it reveals some of the cells in CA1–CA4 regions of the hippocampus. Combining the PSOCT results of hippocampus with higher resolution 2PM autofluorescence images would be super interesting for the study of cell death during neurodegenerative processes such as AD.

For the μ'_b and retardance, we found them to provide complementary information about myelin structure compared to μ_s. Both retardance and μ'_b shows reduced contrast at the crossing fiber region underneath the sulcus in the white matter (Figure 13). And retardance shows enhanced contrast after moderate index matching with 60% glycerol. Besides, both maps highlighted the subcortical U-fibers (Figure 14.a-c), while μ_s was sensitive to myelin density in deep white matter. We used 2PM images to corroborate these measurements. The highly organized U-fibers and densely packed fiber bundles of the deep white matter were recognized by the high resolution autofluorescence of 2PM. The different organizations of fibers in these areas might contribute to variation in these optical parameters. We demonstrated that by combining μ_s, μ'_b and retardance, we are able to provide quantitative measurement about myelin density and fiber structure. In addition, we can validate these mesoscopic measurements from PSOCT with the microscopic information from 2PM for multi-resolution imaging of myelinated fibers.

Lipofuscin, a pigmented substance found within lysosomes or the cytosol of aging cells, has attracted increased attention in the scientific literature as a feature of degeneration. We

demonstrated the visualization of lipofuscin using autofluorescence in the 500–700nm wavelength under 840nm two photon excitation and developed a segmentation method to segment lipofuscin particles from background. The segmented lipofuscin maps were used for quantitative investigation of lipofuscin size, number density and density maps across cortical layers. We used the density map and compared AD, CTE with NC cases and found AD has significantly more lipofuscin (60% more for mean lipofuscin density) at the sulcus of gray matter than NC, while CTE shows minor or no increase of lipofuscin density. We also found both white and gray matter crest has similar density of lipofuscin among these three cases, after using the crest as normalization factor that can remove imaging dependent variations, we found in AD gray matter sulcus has more lipofuscin than gray matter crest, while in NC it's the opposite. This result suggests that the gray matter sulcus is most affected by AD pathology in the perspective of lipofuscin accumulation. Our results are mostly in agreement with lipofuscin measurement in the last century when multiple groups of researchers found no or slightly more lipofuscin in AD comparing to NC. However, they were limited to the imaging techniques available then and only investigated around 100 neurons, while we covered 2x2x0.1cm brain region and hence our results bear more statistical significance. Consequently, our system will be useful to investigate in-depth differences in lipofuscin distribution between different neurodegenerative processes.

Besides, lipofuscin is thought to be related to the NFT through the PN, a protecting structure of neurons in the ECM. NFT is one of the pathological hallmarks in AD and CTE, which requires complex method for imaging and measuring. Thus, better quantitative

measurement of NFT will facilitate the investigation of AD. By comparing to histology of NFT, our system can validate the spatial relationship between NFT and lipofuscin. And if these two structures do share common spatial distribution, our system can be used for label-free measurement of NFT using lipofuscin.

Lipofuscin was not the sole source of autofluorescence; elastin and collagen in the extracellular matrix[95] also contribute to autofluorescence. Interestingly, we found dark spots in the 435–485nm wavelength channel (Figure 16 and Figure 17) that colocalize with lipofuscin. By comparing with Nissl stain we found this lipofuscin-dark-spot structure shows strong correspondence with neuron soma, suggesting that the method might be useful as a neuron counting strategy [96]. Although the validation and quantification of autofluorescence was conducted at sub-micro resolution by a separate 2PM in this study, recent advancements in machine learning methods show promise as a means of segmenting low-resolution images using prior knowledge from high-resolution ones[64,65]. Cell death is discovered in multiple neurodegenerative processes, among them the most interesting case is the cell death in hippocampus in AD[91]. Combining with the μ_s map, we believe our method of cell identifying and counting will facilitate the high-throughput study of cell death in hippocampus.

We discussed another application of our method which is imaging the capillaries in the human brain and quantitatively calculate the vessel density between disease cases and normal controls. PSOCT and 2PM provided complementary images of vessels at different

resolutions that enrichened the vascular images obtained from the individual modalities. Specifically, PSOCT has been shown to reconstruct 3D vascular structures in a large volume, allowing for vessel tracking and segmentation at the mesoscopic resolution. Yang et al.[14] segmented vascular structures from the OCT volumetric images and developed quantitative metrics for characterizing the geometric properties of vascular structures. 2PM provided microscopic images that revealed smaller vessels and capillaries that are beyond the resolution limit of PSOCT. Capillary disease is at the focus of vascular abnormality study[81,82]. With robust segmentation method of the capillaries in 2PM images, we believe our method can enable high-throughput imaging of large vessels and capillaries for the study of decline in the integrity of the vascular system.

There are several limitations to our method. First, while combining 2PM with PSOCT allowed for the visualization of smaller vessels and capillaries, 2PM was performed at a single depth integrating over 48 μm of the tissue, about one third of PSOCT depth of focus. Therefore, there will be information mismatch between the co-registered PSOCT and 2PM images. This imaging strategy also precluded a full volumetric reconstruction from 2PM images. To overcome the problem, depth scanning is needed at a cost of longer acquisition time. But for small sample size, this will only result in the extension of one-day experiment into a week or so, which is acceptable. Second, to resolve even smaller structures such as individual axons, myelin sheaths, the full capillary bed, and small cells, a sub-micron resolution is necessary, which is not this hybrid system designed for. Hence, combination with other high resolution microscope systems is necessary for that purpose.

In summary, our method enabled scalable and multi-resolution investigation of myelin content, lipofuscin, cell density, large vessels and capillaries in the human brain. And all these structures are imaged without distortion and can be easily registered. Consequently, our method offers a powerful tool to help understand brain anatomy as well as neurological disorders and neurodegeneration.

BIBLIOGRAPHY

1. McConnell, S. K. The generation of neuronal diversity in the central nervous system. *Annual Review of Neuroscience.* **14,** 269–300, (1991). https://doi.org/10.1146/annurev.ne.14.030191.001413

2. Jiang, X. *et al.* Principles of connectivity among morphologically defined cell types in adult neocortex. *Science.* **350**(6264), aac9462, (2015). https://doi.org/10.1126/science.aac9462

3. Herford, A. S. Regeneration and Beyond. *Oral & Maxillofacial Surgery Clinics of North America.* **29**(1), ix (2017). https://doi.org/10.1016/j.coms.2016.10.001

4. Li, J. *et al.* Astrocytes in oligodendrocyte lineage development and white matter pathology. *Frontiers in Cellular Neuroscience.* **10**, 1–13 (2016).

5. Barkovich, A. J., Lyon, G. & Evrard, P. Formation, maturation, and disorders of white matter. *AJNR. American Journal of Neuroradiology.* **13**, 447–461 (1992).

6. Stadelmann, C., Timmler, S., Barrantes-Freer, A. & Simons, M. Myelin in the central nervous system: Structure, function, and pathology. *Physiological Reviews.* **99**, 1381–1431 (2019).

7. Peterson, E. C., Wang, Z. & Britz, G. Regulation of cerebral blood flow. *International Journal of Vascular Medicine.* **2011**, (2011).

8. Evans, A. C., Janke, A. L., Collins, D. L. & Baillet, S. Brain templates and atlases. *NeuroImage* **62**, 911–922 (2012).

9. Revell, A. Y. *et al.* A framework For brain atlases: Lessons from seizure dynamics. *NeuroImage* **254**, 118986 (2022).

10. Miletić, S. *et al.* Charting human subcortical maturation across the adult lifespan with in vivo 7 T MRI. *NeuroImage* **249**, 118872 (2022).

11. Amunts, K. *et al.* BigBrain: An ultrahigh-resolution 3D human brain model. *Science.* **340**, 1472–1475 (2013).

12. Lefebvre, J., Castonguay, A., Pouliot, P., Descoteaux, M. & Lesage, F. Whole mouse brain imaging using optical coherence tomography: reconstruction, normalization, segmentation, and comparison with diffusion MRI. *Neurophotonics* **4**, 041501 (2017).

13. Li, T., Liu, C. J. & Akkin, T. Contrast-enhanced serial optical coherence scanner with deep learning network reveals vasculature and white matter organization of mouse brain. *Neurophotonics* **6**, 035004 (2019). https://doi.org/10.1117/1.nph.6.3.035004

14. Yang, J. *et al.* Volumetric characterization of microvasculature in ex vivo human brain samples by serial sectioning optical coherence tomography. *IEEE Transactions on Bio-medical Engineering.* **69**, 3645–3656 (2022).

15. Wang, H., Lenglet, C. & Akkin, T. Structure tensor analysis of serial optical coherence scanner images for mapping fiber orientations and tractography in the brain. *Journal of Biomedical Optics.* **20**, 036003 (2015).

16. Wang, H. *et al.* Polarization sensitive optical coherence microscopy for brain imaging. *Optics Letters.* **41**, 2213 (2016).

17. Fan, C. & Yao, G. Imaging myocardial fiber orientation using polarization sensitive optical coherence tomography. *Biomedical Optics Express* **4**, 460 (2013).

18. Wang, H. *et al.* as-PSOCT : Volumetric microscopic imaging of human brain architecture and connectivity. *NeuroImage* **165**, 56–68 (2018).

19. Shirshin, E. A. *et al.* Two-photon autofluorescence lifetime imaging of human skin papillary dermis in vivo: Assessment of blood capillaries and structural proteins localization. *Scientific Reports.* **7**, 1–10 (2017).

20. Kim, B. *et al.* In vivo visualization of skin inflammation by optical coherence tomography and two-photon microscopy. *Biomedical Optics Express* **6**, 2512 (2015).

21. La Schiazza, O. & Bille, J. F. High-speed two-photon excited autofluorescence imaging of ex vivo human retinal pigment epithelial cells toward age-related macular degeneration diagnostic. *Journal of Biomedical Optics.* **13**, 064008 (2008).

22. Teng, S. W. *et al.* Multiphoton autofluorescence and second-harmonic generation imaging of the ex vivo porcine eye. *Investigative Ophthalmology & Visual Science.* **47**, 1216–1224 (2006).

23. Fukumura, D. & Jain, R. K. Tumor microvasculature and microenvironment: Targets for anti-angiogenesis and normalization. *Microvascular Research.* **74**, 72–84 (2007).

24. König, K. *et al.* Clinical optical coherence tomography combined with multiphoton tomography of patients with skin diseases. *Journal of Biophotonics* **2**,

389–397 (2009).

25. Kantelhardt, S. R. *et al.* Multi-photon excitation fluorescence microscopy of brain-tumour tissue and analysis of cell density. *Acta Neurochirurgica* **151**, 253–262 (2009).

26. Poulon, F. *et al.* Real-time Brain Tumor imaging with endogenous fluorophores: a diagnosis proof-of-concept study on fresh human samples. *Scientific Reports.* **8**, 1–11 (2018).

27. Kretschmer, S. *et al.* Autofluorescence multiphoton microscopy for visualization of tissue morphology and cellular dynamics in murine and human airways. *Laboratory Investigation.* **96**, 918–931 (2016).

28. Shrirao, A. B. *et al.* Autofluorescence of blood and its application in biomedical and clinical research. *Biotechnology and Bioengineering.* **118**, 4550–4576 (2021).

29. Moreno-García, A., Kun, A., Calero, O., Medina, M. & Calero, M. An overview of the role of lipofuscin in age-related neurodegeneration. *Frontiers in Neuroscience.* **12**, 1–13 (2018).

30. Yeh, A. T. *et al.* Imaging wound healing using optical coherence tomography and multiphoton microscopy in an in vitro skin-equivalent tissue model. *Journal of Biomedical Optics.* **9**, 248 (2004).

31. Gagnon, L. *et al.* Multimodal reconstruction of microvascular-flow distributions using combined two-photon microscopy and Doppler optical coherence tomography. *Neurophotonics* **2**, 015008 (2015).

32. Braaf, B. *et al.* Phase-stabilized optical frequency domain imaging at 1-μm for the measurement of blood flow in the human choroid. *Optics Express* **19**, 20886 (2011).

33. Ragan, T. *et al.* Serial two-photon tomography for automated ex vivo mouse brain imaging. *Nature Methods* **9**, 255–258 (2012).

34. Fu, X. *et al.* Design of an ultrafast oscillating blade microtome based on vibration cancellation. *Proceedings of the 35th Annual Meetings of the ASPE.* **73**, 38–42 (2020).

35. Wang, J., Li, C. & Chen, S. C. Sectioning soft materials with an oscillating blade. *Precision Engineering.* **56**, 96–100 (2019).

36. Yun, S. H., Tearney, G. J., Bouma, B. E., Park, B. H. & F, J. de Boer, 'High-speed spectral domain optical coherence tomography at 1.3 μm wavelength,' *Optics*

Express **11**, 3598–3604 (2003).

37. Peng, T. *et al.* A BaSiC tool for background and shading correction of optical microscopy images. *Nature Communications.* **8**, 1–7 (2017).

38. Vermeer, K. A., Mo, J., Weda, J. J. A., Lemij, H. G. & de Boer, J. F. Depth-resolved model-based reconstruction of attenuation coefficients in optical coherence tomography. *Biomedical Optics Express* **5**, 322 (2014).

39. Friedrich, P. *et al.* The Relationship between Axon Density, Myelination, and Fractional Anisotropy in the Human Corpus Callosum. *Cerebral Cortex* **30**, 2042–2056 (2020).

40. Blanke, N., Go, V., Rosene, D. L. & Bigio, I. J. Quantitative birefringence microscopy for imaging the structural integrity of CNS myelin following circumscribed cortical injury in the rhesus monkey. *Neurophotonics* **8**, (2021).

41. Pistorio, A. L., Hendry, S. H. & Wang, X. A modified technique for high-resolution staining of myelin. *Journal of Neuroscience Methods* **153**, 135–146 (2006).

42. Macenko, M. *et al.* A method for normalizing histology slides for quantitative analysis. *2009 IEEE International Symposium on Biomedical Imaging: From Nano to Macro*, Boston, MA, USA, 2009, pp. 1107–1110 (2009). doi:10.1109/ISBI.2009.5193250

43. Augustinack, J. C. *et al.* MRI parcellation of ex vivo medial temporal lobe. *NeuroImage* **23**, 1–7 (2013).

44. Mourant, J. R., Fuselier, T., Boyer, J., Johnson, T. M. & Bigio, I. J. Predictions and measurements of scattering and absorption over broad wavelength ranges in tissue phantoms. *Applied Optics* **36**, 949 (1997).

45. Suárez-Solá, M. L., Francisco J. González-Delgado, M. P.-M., Medina-Bolívar, O. C., Hernández-Acosta, N. C. & Miriam González-Gómez and Gundela Meyer. Neurons in the white matter of the adult human neocortex. *Frontiers in Neuroanatomy* **3**, 1–7 (2009). https://doi.org/10.3389/neuro.05.007.2009

46. Balaram, P., Young, N. A. & Kaas, J. H. Histological features of layers and sublayers in cortical visual areas V1 and V2 of chimpanzees, macaque monkeys, and humans. *Eye and Brain* **6**, 5–18 (2014).

47. Bashkatova, T. A., Bashkatov, A. N., Kochubey, V. I. & Tuchin, V. V. Light scattering properties for spherical and cylindrical particles: a simple approximation derived from Mie calculations. *Saratov Fall Meeting 2000: Optical Technologies*

in Biophysics and Medicine II, Proceedings of SPIE, **4241**, 247–259 (2001). doi:10.1117/12.431529

48. Pusterla, J. M., Malfatti-Gasperini, A. A., Puentes-Martinez, X. E., Cavalcanti, L. P. & Oliveira, R. G. Refractive index and thickness determination in Langmuir monolayers of myelin lipids. *Biochimica et Biophysica Acta - Biomembranes* **1859**, 924–930 (2017).

49. Bai, B. *et al.* Deep learning-enabled virtual histological staining of biological samples. *Light, Science & Applications.* **12**, 57 (2023). https://doi.org/10.1038/s41377-023-01104-7

50. Pang, C. C. C., Kiecker, C., O'Brien, J. T., Noble, W. & Chang, R. C. C. Ammon's Horn 2 (CA2) of the Hippocampus: A Long-Known Region with a New Potential Role in Neurodegeneration. *Neuroscientist* **25**, 167–180 (2019).

51. Wang, H., Magnain, C., Sakadžić, S., Fischl, B. & Boas, D. A. Characterizing the optical properties of human brain tissue with high numerical aperture optical coherence tomography. *Biomedical Optics Express* **8**, 5617 (2017).

52. Magnain, C. *et al.* Colocalization of neurons in optical coherence microscopy and Nissl-stained histology in Brodmann's area 32 and area 21. *Brain Structure & Function* **224**, 351–362 (2019).

53. Kut, C. *et al.* Detection of Human Brain Cancer Infiltration ex vivo and in vivo Using Quantitative Optical Coherence Tomography. *Physiology & Behavior* **63**, 1–18 (2014).

54. Yashin, K. S. *et al.* Cross-polarization optical coherence tomography for brain tumor imaging. *Frontiers in Oncology* **9**, 201 (2019). https://doi.org/10.3389/fonc.2019.00201

55. Brunk, U. T. & Terman, A. The mitochondrial-lysosomal axis theory of aging: Accumulation of damaged mitochondria as a result of imperfect autophagocytosis. *European Journal of Biochemistry* **269**, 1996–2002 (2002).

56. Brückner, G. *et al.* Cortical areas abundant in extracellular matrix chondroitin sulphate proteoglycans are less affected by cytoskeletal changes in Alzheimer's disease. *Neuroscience* **92**, 791–805 (1999).

57. Dowson, J. H. Neuronal lipofuscin accumulation in ageing and Alzheimer dementia: A pathogenic mechanism? *British Journal of Psychiatry* **140**, 142–148 (1982).

58. Chen, C. *et al.* In Vivo Near-Infrared Two-Photon Imaging of Amyloid Plaques in Deep Brain of Alzheimer's Disease Mouse Model. *ACS Chemical Neuroscience* **9**, 3128–3136 (2018).

59. De Biase, D. *et al.* Amyloid precursor protein, lipofuscin accumulation and expression of autophagy markers in aged bovine brain. *BMC Veterinary Research* **13**, 1–9 (2017).

60. Gray, D. A. & Woulfe, J. Lipofuscin and aging: a matter of toxic waste. *Science of Aging Knowledge Environment* **2005**, 1–6 (2005).

61. D'Andrea, M. R. *et al.* Lipofuscin and Aβ42 exhibit distinct distribution patterns in normal and Alzheimer's disease brains. *Neuroscience Letters* **323**, 45–49 (2002).

62. Brizzee, K. R. & Johnson, F. A. Depth distribution of lipofuscin pigment in cerebral cortex of albino rat. *Acta Neuropathologica* **16**, 205–219 (1970).

63. Mann, D. M. A., Yates, P. O. & Marcyniuk, B. Changes in nerve cells of the nucleus basalis of Meynert in Alzheimer's disease and their relationship to ageing and to the accumulation of lipofuscin pigment. *Mechanisms of Ageing & Development.* **25**, 189–204 (1984).

64. Li, X. *et al.* Unsupervised content-preserving transformation for optical microscopy. *Light, Science and Applications* **10**, (2021).

65. Eun, D. in *et al.* Deep-learning-based image quality enhancement of compressed sensing magnetic resonance imaging of vessel wall: comparison of self-supervised and unsupervised approaches. *Scientific Reports* **10**, 1–17 (2020).

66. Morawski, M., Brückner, M. K., Riederer, P., Brückner, G. & Arendt, T. Perineuronal nets potentially protect against oxidative stress. *Experimental Neurology* **188**, 309–315 (2004).

67. Bartzokis, G. Age-related myelin breakdown: A developmental model of cognitive decline and Alzheimer's disease. *Neurobiology of Aging* **25**, 5–18 (2004).

68. Bartzokis, G. *et al.* White matter structural integrity in healthy aging adults and patients with Alzheimer disease: A magnetic resonance imaging study. *Archives of Neurology* **60**, 393–398 (2003).

69. Wallin, A., Gottfries, C. G., Karlsson, I. & Svennerholm, L. Decreased myelin lipids in Alzheimer's disease and vascular dementia. *Acta Neurologica Scandinavica* **80**, 319–323 (1989).

70. Goldstein, L. E. *et al.* Chronic traumatic encephalopathy in blast-exposed military veterans and a blast neurotrauma mouse model. *Science Translational Medicine* **4** (134), 134ra60 (2012). https://doi.org/10.1126/scitranslmed.3003716

71. Taber, K. H., Warden, D. L. & Hurley, R. A. Blast-related traumatic brain injury: What is known? *Journal of Neuropsychiatry and Clinical Neurosciences.* **18**, 141–145 (2006).

72. Laule, C. *et al.* Myelin water imaging of multiple sclerosis at 7 T: Correlations with histopathology. *NeuroImage* **40**, 1575–1580 (2008).

73. Kelsey C. Martin Mhatre V. Ho, J.-A. L. *et al.* The effects of healthy aging on intracerebral blood vessels visualized by magnetic resonance angiography. *Bone* **23**, 1–7 (2008).

74. Thore, C. R. *et al.* Morphometric analysis of arteriolar tortuosity in human cerebral white matter of preterm, young, and aged subjects. *Journal of Neuropathology and Experimental Neurology* **66**, 337–345 (2007).

75. Fischer, V. W., Siddiqi, A. & Yusufaly, Y. Altered angioarchitecture in selected areas of brains with Alzheimer's disease. *Acta Neuropathologica* **79**, 672–679 (1990).

76. Ambrose, C. T. Neuroangiogenesis: A vascular basis for Alzheimer's disease and cognitive decline during aging. *Journal of Alzheimer's Disease* **32**, 773–788 (2012).

77. Farkas, E. & Luiten, P. G. M. Cerebral microvascular pathology in aging and Alzheimer's disease. *Progress in Neurobiology* **64**, (2001).

78. Mhatre V. Ho, Ji-Ann Lee, and K. C. M. & Dien et al., 2013. Direct labeling and visualization of blood vessels with lipophilic carbocyanine dye DiI. *Bone* **23**, 1–7 (2008).

79. Brown, W. R. & Thore, C. R. Review: Cerebral microvascular pathology in ageing and neurodegeneration. *Neuropathology and Applied Neurobiology* **37**, 56–74 (2011).

80. Yang, J. *et al.* Volumetric Characterization of Microvasculature in Ex Vivo Human Brain Samples By Serial Sectioning Optical Coherence Tomography. *IEEE Transactions on Bio-medical. Engineering* **69**, 3645–3656 (2022).

81. Watanabe, C. *et al.* Aging of the Vascular System and Neural Diseases. *Frontiers in Aging Neuroscience* **12**, 1–9 (2020). https://doi.org/10.3389/fnagi.2020.557384

82. Brown, W. R., Moody, D. M., Thore, C. R., Challa, V. R. & Anstrom, J. A. Vascular dementia in leukoaraiosis may be a consequence of capillary loss not only in the lesions, but in normal-appearing white matter and cortex as well. *Journal of the Neurological Sciences* **257**, 62–66 (2007).

83. Moccia, S., De Momi, E., El Hadji, S. & Mattos, L. S. Blood vessel segmentation algorithms — Review of methods, datasets and evaluation metrics. *Computer Methods and Programs in Biomedicine* **158**, 71–91 (2018).

84. Nirmala, J. G. & Lopus, M. Cell death mechanisms in neurodegeneration. *Cell Biology and Toxicology* **36**, 145–164 (2020).

85. Kelly, J. G. & Hawken, M. J. Quantification of neuronal density across cortical depth using automated 3D analysis of confocal image stacks. *Brain Structure & Function* **222**, 3333–3353 (2017).

86. Niikura, T., Tajima, H. & Kita, Y. Neuronal Cell Death in Alzheimers Disease and a Neuroprotective Factor, Humanin. *Current Neuropharmacology* **4**, 139–147 (2006).

87. Naoi, M. & Maruyama, W. Cell death of dopamine neurons in aging and Parkinson's disease. *Mechanisms of Ageing and Development* **111**, 175–188 (1999).

88. Jakel, R. J. & Maragos, W. F. Neuronal cell death in Huntington's disease: A potential role for dopamine. *Trends in Neurosciences.* **23**, 239–245 (2000).

89. Andrade-Moraes, C. H. *et al.* Cell number changes in Alzheimer's disease relate to dementia, not to plaques and tangles. *Brain* **136**, 3738–3752 (2013).

90. Magnain, C. *et al.* Optical coherence tomography visualizes neurons in human entorhinal cortex. *Neurophotonics* **2**, 015004 (2015).

91. Rao, Y. L. *et al.* Hippocampus and its involvement in Alzheimer's disease: a review. *3 Biotech* **12**, 1–10 (2022).

92. McKee, A. C., Stein, T. D., Kiernan, P. T. & Alvarez, V. E. The neuropathology of chronic traumatic encephalopathy. *Brain Pathology.* **25**, 350–364 (2015).

93. Metaxas, A. & Kempf, S. J. Neurofibrillary tangles in Alzheimer's disease: Elucidation of the molecular mechanism by immunohistochemistry and tau protein phospho-proteomics. *Neural Regeneration Research* **11**, 1579–1581 (2016).

94. Moloney, C. M., Lowe, V. J. & Murray, M. E. Visualization of neurofibrillary tangle maturity in Alzheimer's disease: A clinicopathologic perspective for

biomarker research. *Alzheimer's & Dementia* **17**, 1554–1574 (2021).

95. Karamanos, N. K. *et al.* A guide to the composition and functions of the extracellular matrix. *FEBS Journal.* **288**, 6850–6912 (2021).

96. Magnain, C., Augustinack, J. C., Martin, R., Boas, D. A. & Fischl, B. Blockface Histology with Optical Coherence Tomography: A Comparison with Nissl Staining. *NeuroImage* **23**, 1–7 (2014).

CURRICULUM VITAE